



HAL
open science

Processes controlling magma fertility at buenavista del cobre porphyry copper deposit (cananea, méxico): A new petrogenetic model based on zircon u-pb dating and apatite geochemistry

Víctor Almada-Gutiérrez, Mélanie Noury, Thierry Calmus, Nathan Cogné,
Edgardo Barrera-Moreno, Marc Poujol

► To cite this version:

Víctor Almada-Gutiérrez, Mélanie Noury, Thierry Calmus, Nathan Cogné, Edgardo Barrera-Moreno, et al.. Processes controlling magma fertility at buenavista del cobre porphyry copper deposit (cananea, méxico): A new petrogenetic model based on zircon u-pb dating and apatite geochemistry. *Ore Geology Reviews*, 2024, 175, pp.106320. 10.1016/j.oregeorev.2024.106320 . insu-04768553

HAL Id: insu-04768553

<https://insu.hal.science/insu-04768553v1>

Submitted on 6 Nov 2024

HAL is a multi-disciplinary open access archive for the deposit and dissemination of scientific research documents, whether they are published or not. The documents may come from teaching and research institutions in France or abroad, or from public or private research centers.

L'archive ouverte pluridisciplinaire **HAL**, est destinée au dépôt et à la diffusion de documents scientifiques de niveau recherche, publiés ou non, émanant des établissements d'enseignement et de recherche français ou étrangers, des laboratoires publics ou privés.



Distributed under a Creative Commons Attribution - NonCommercial - NoDerivatives 4.0
International License

Journal Pre-proofs

Processes controlling magma fertility at buenavista del cobre porphyry copper deposit (cananea, méxico): A new petrogenetic model based on zircon u-pb dating and apatite geochemistry

Víctor Almada-Gutiérrez, Mélanie Noury, Thierry Calmus, Nathan Cogné, Edgardo Barrera-Moreno, Marc Poujol

PII: S0169-1368(24)00453-0
DOI: <https://doi.org/10.1016/j.oregeorev.2024.106320>
Reference: OREGEO 106320

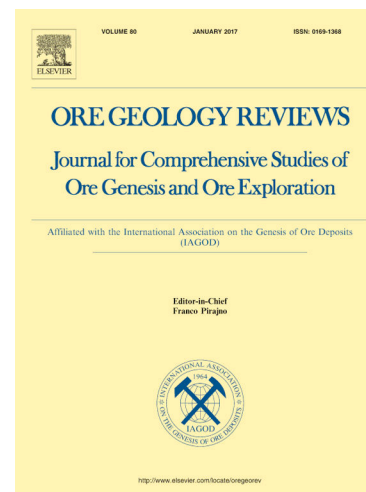
To appear in: *Ore Geology Reviews*

Received Date: 17 May 2024
Revised Date: 24 September 2024
Accepted Date: 29 October 2024

Please cite this article as: V. Almada-Gutiérrez, M. Noury, T. Calmus, N. Cogné, E. Barrera-Moreno, M. Poujol, Processes controlling magma fertility at buenavista del cobre porphyry copper deposit (cananea, méxico): A new petrogenetic model based on zircon u-pb dating and apatite geochemistry, *Ore Geology Reviews* (2024), doi: <https://doi.org/10.1016/j.oregeorev.2024.106320>

This is a PDF file of an article that has undergone enhancements after acceptance, such as the addition of a cover page and metadata, and formatting for readability, but it is not yet the definitive version of record. This version will undergo additional copyediting, typesetting and review before it is published in its final form, but we are providing this version to give early visibility of the article. Please note that, during the production process, errors may be discovered which could affect the content, and all legal disclaimers that apply to the journal pertain.

© 2024 Published by Elsevier B.V.



1 **PROCESSES CONTROLLING MAGMA FERTILITY AT BUENAVISTA DEL**
 2 **COBRE PORPHYRY COPPER DEPOSIT (CANANEA, MÉXICO): A NEW**
 3 **PETROGENETIC MODEL BASED ON ZIRCON U-PB DATING AND APATITE**
 4 **GEOCHEMISTRY**

5 Víctor Almada-Gutiérrez^{1,2,3*}, Mélanie Noury^{1,3}, Thierry Calmus^{1,3}, Nathan Cogné⁴, Edgardo
 6 Barrera-Moreno⁵, Marc Poujol⁴

7
 8 ¹Estación Regional del Noroeste, Instituto de Geología, Universidad Nacional Autónoma de
 9 México, Hermosillo, Sonora, México

10 ²Posgrado en Ciencias de la Tierra, Estación Regional del Noroeste, Instituto de Geología,
 11 Universidad Nacional Autónoma de México, Hermosillo, Sonora, México

12 ³Laboratorio Nacional de Geoquímica y Mineralogía (LANGEM), Instituto de Geología,
 13 Universidad Nacional Autónoma de México, Hermosillo, Sonora, México

14 ⁴Univ. Rennes, CNRS, Géosciences Rennes, UMR6118, F-35000 Rennes, France

15 ⁵Buenavista del Cobre, Superintendencia de Geología, Grupo México, Cananea, Sonora,
 16 México

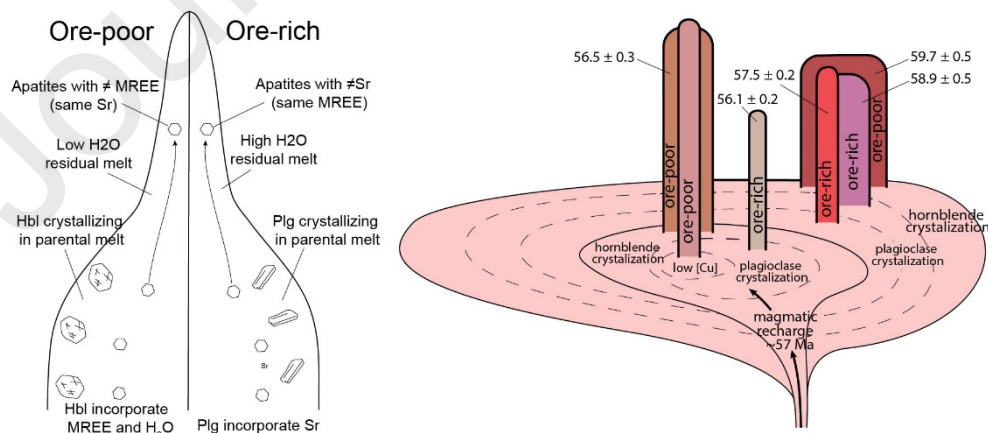
17 *Corresponding author: mnoury@geologia.unam.mx

18

19 **KEYWORDS**

20 porphyry copper deposit, magma fertility, apatite geochemistry, geochronology, Cananea
 21 mine, Mexico

22 **GRAPHICAL ABSTRACT**



23

24 HIGHLIGHTS

- 25 - Zircon U-Pb dating of the ore-related porphyries indicates a life span of at least ~4 Myr
26 for the magmatic activity related to the mineralization processes at the Buenavista del
27 Cobre deposit
- 28 - At least two magmatic cycles involving fractional crystallization of plagioclase at depth
29 are associated with the formation of the giant Buenavista del Cobre deposit
30 mineralization.
- 31 - Apatite geochemistry can be used as an exploration tool to differentiate ore-rich from
32 ore-poor porphyry intrusions analyzing apatite REE signatures.

33

34 ABSTRACT

35 The Buenavista del Cobre is a world-class porphyry Cu-Mo deposit located in the Cananea
36 Mining District, northern Sonora, México. Using zircon U-Pb dating, we show that the
37 Proterozoic Cananea Granite, unconformably overlain regionally by Paleozoic limestones
38 hosting skarn deposits underlies the present-day pit. We also present new crystallization ages
39 for host rocks of copper mineralization in the District, dating for the first time a volcanic rock
40 of the Henrietta Formation at $186.8 \pm 1.1/3.0$ Ma and the El Torre Syenite at $176.3 \pm 1.1/2.9$
41 Ma. Zircon U-Pb dating of the different porphyritic bodies reveals that the magmatic activity
42 at Buenavista del Cobre lasted at least 4 Myr, from $59.7 \pm 0.5/1.1$ Ma to $56.1 \pm 0.2/0.9$ Ma.
43 The deposit is composed by several porphyry intrusions referred to as “ore-rich” and “ore-
44 poor” based on their individual metal contributions, which provides the opportunity to study
45 the origin and processes enhancing magma fertility in an individual deposit. Combining our
46 new geochronological dataset with geochemistry of apatite from the different porphyries
47 allows us to propose a new petrogenetic model for the Buenavista del Cobre deposit. As the
48 apatite Eu and Ce anomalies overlap with no clear difference between the ore-rich and ore-
49 poor intrusions, we propose that the magmatic oxidation states of the magmas were similar.
50 However, differences in apatite REE signatures, as well as variations in apatite Sr
51 compositions between the two groups suggest that fractional crystallization processes in the
52 parental magma influence the fertility of the porphyries. Additionally, apatite Cl contents of
53 ore-rich porphyry intrusions are higher (>0.4 wt%) than the ore-poor intrusions (<0.2 wt%),
54 suggesting an important role of the initial Cl content of the magmas in the mineralization
55 process. These observations give new insights on the petrogenetic processes at origin of
56 porphyry magma fertility. We propose that the evolution of the parental melt by fractional
57 crystallization of hydrous minerals (hornblende) at upper crustal levels induced low H₂O
58 content of the residual magma, resulting in the formation of ore-poor porphyries. In contrast,
59 we suggest that fractionation of anhydrous minerals (plagioclase) increased the H₂O content
60 in the residual melt, leading to the formation of ore-rich porphyries. Our new data allow us
61 to propose an original genetic model for the Buenavista del Cobre deposit, which involves
62 two cycles of supply, cooling and partial crystallization. This contribution shows that
63 petrogenetic processes controlling porphyry copper magmas fertility are recorded in the
64 composition of apatite at the deposit scale and highlights the importance of considering
65 apatite geochemistry as an exploration tool.

66

67

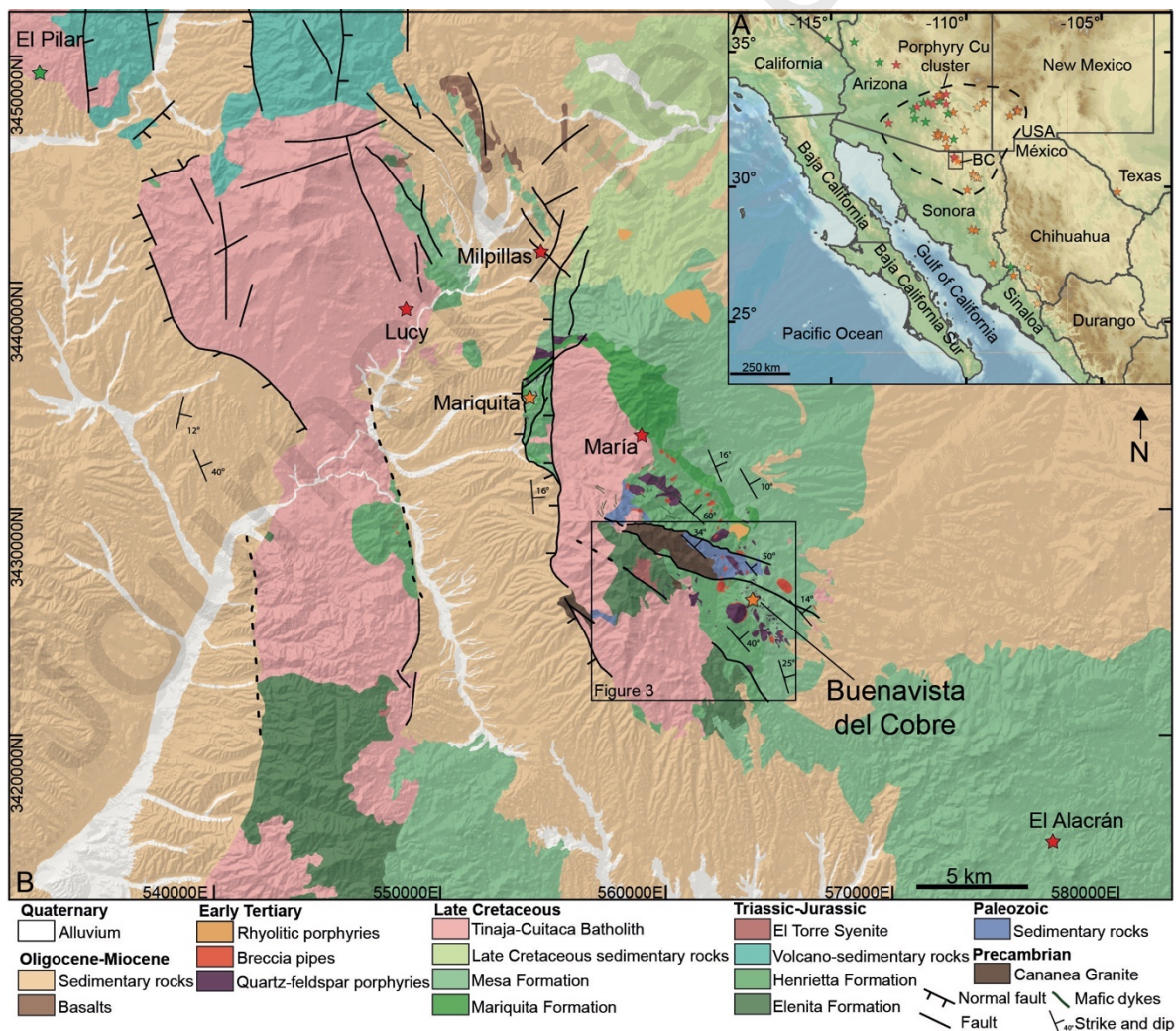
68 1. Introduction

69 Porphyry copper deposits around the world are commonly associated with subduction-related
70 magmatism and are typically the product of superposition of multiple porphyry intrusions
71 (e.g., Proffett, 2003; Sillitoe, 2010). Zircon U-Pb geochronology studies indicate that the
72 time span for the emplacement of porphyry intrusions in some giant deposits is ~2 to ~5 Myr
73 (e.g., Ballard et al., 2001; Makshev et al., 2004; Harris et al., 2008). At the deposit scale, each
74 porphyry intrusion contributes to the total metal budget of the deposit and are often labelled
75 as “ore-rich” or “ore-poor” intrusions based on their individual metal contribution. Fertility
76 of an intrusion is believed to be controlled by the oxidation state and by the H₂O and volatile
77 contents of the magma (Richards, 2003 and 2011; Sillitoe, 2010). The influence of these
78 parameters on magma fertility has been tested by analyzing and comparing ore-related versus
79 ore-barren intrusions on a global and regional scale (e.g., Lang and Titley 1998; Loucks
80 2014). However, at the deposit scale, the processes controlling the fertility of the different
81 porphyry intrusions at the origin of ore-poor and ore-rich intrusions remain unclear.

82 The Buenavista del Cobre deposit (formerly Cananea mine) is a world-class porphyry Cu-
83 Mo deposit located in the center of the Cananea Mining District in northern Sonora, Mexico
84 (Fig. 1). It is the largest Cu/Mo producer in the district with tonnages of 7,140 Mt grading
85 0.42% Cu and 0.008% Mo (Singer et al., 2005). The Cananea Mining District is part of the
86 Arizona-Sonora-New Mexico cluster of porphyry Cu deposits, which were emplaced from
87 the Late Cretaceous to the Eocene (Keith and Swan, 1995; Leveille and Stegen, 2012;
88 Valencia-Moreno et al., 2016; Fig. 1). Several porphyry phases have been recognized in the
89 Buenavista del Cobre deposit, which are distinguished by their cross-cutting relationships,
90 mineralogical compositions and textures (Valentine, 1936; Ochoa-Landín and Echávarri-
91 Pérez, 1978; Ochoa-Landín and Navarro-Meyer, 1979). It has been long recognized that
92 some of these intrusions have a more important metal contribution than others and were
93 therefore labelled as either ore-rich or ore-poor porphyry intrusions (Ochoa-Landín and
94 Navarro-Meyer, 1979). In particular, the La Colorada and 755 porphyries are associated with
95 significant contributions of Cu and Mo sulfides to the porphyry system (Ochoa-Landín and
96 Navarro-Meyer, 1979; Correa-García, 1983). On the other hand, the Feldspar and 8-110
97 porphyries are associated with low-Cu grade breccias and the Coarse-grained Porphyry unit
98 is referenced as “barren” (Ochoa-Landín and Navarro-Meyer, 1979; Correa-García, 1983),
99 but presents scarce sulfide mineralization. In the following, we thus refer to the La Colorada
100 and 755 porphyries as “ore-rich intrusions” and to the Feldspar, 8-110 and Coarse-grained
101 porphyries as “ore-poor intrusions”. A comparison of the geochemical characteristics of “ore-
102 poor” and “ore-rich” intrusions at Buenavista del Cobre can provide insights into the
103 petrogenetic processes that led to their formation. However, the intense hydrothermal
104 alteration associated with porphyry copper deposits prevents the assessment of the
105 petrogenetic processes controlling the magma fertility using classical whole rock
106 geochemistry.

107 Yet, apatite geochemistry has recently been used to assess metallogenetic fertility of different
 108 mineral deposits at a regional scale as well as the role of the magmatic processes involved in
 109 their formation (e.g., Belousova et al., 2001 and 2002; Cao et al., 2012; Mao et al., 2016).
 110 Apatite incorporates geologically valuable elements that are sensitive to the evolution of
 111 magmas, such as rare-earth elements (REE), Sr, Y, Th and U (e.g., Sha and Chappell, 1999;
 112 Piccoli and Candela, 2002; Prowatke and Klemme, 2006; Bruand et al., 2017). Also, it has
 113 recently been proposed as a porphyry indicator mineral (PIMS) because it records magmatic
 114 and hydrothermal processes associated with the formation of porphyry copper deposits (e.g.,
 115 Loader, 2017; Bouzari et al., 2017).

116 This study aims to characterize the chronology and the petrogenetic processes at the origin
 117 of the ore-poor and ore-rich porphyritic bodies associated with Cu-Mo mineralization in the
 118 Buenavista del Cobre deposit. To this end, we dated the crystallization ages of the porphyry
 119 intrusions related to the different magmatic events that generated the mineralization. In
 120 addition, we used apatite trace element compositions as a proxy to identify the petrogenetic
 121 processes involved in the formation of ore-rich and ore-poor porphyry intrusions and to
 122 evaluate the role of the oxidation state and volatile content of these magmas in the
 123 mineralization process.



125 Figure 1. Location and regional geological setting of the Cananea Mining District. Stars
 126 indicate the location of the main porphyry copper deposits, their colors corresponding to the
 127 age ranges of emplacement: green= 75-65 Ma, red= 65-60 Ma, orange= 60-55 Ma, and
 128 yellow= 55-40 Ma. A) Porphyry Cu deposits province of southwestern North America.
 129 Dotted lines indicate the limit of the porphyry copper cluster of Arizona-Sonora-New Mexico
 130 (after Del Rio Salas et al., 2017). BC= Buenavista del Cobre deposit. B) Regional geological
 131 map of the Cananea Mining District, modified from Noguez-Alcántara (2008) and Del Rio-
 132 Salas et al. (2017).

133

134

135

136 **2. Geological background**

137 **2.1. Regional geological setting**

138 The Cananea Mining District consists of several porphyry copper deposits, including El Pilar,
 139 Milpillas, Lucy, Mariquita, María, Buenavista del Cobre Cu-Mo deposits and the El Alacrán
 140 prospect (Fig. 1). The basement of the District is represented by the Precambrian Cananea
 141 anorogenic Granite (1.44 Ga; Anderson and Silver, 1977; Fig. 1) that intruded the
 142 Precambrian metamorphic rocks of the Mazatzal province (Anderson and Silver, 1981; Eisele
 143 and Isachsen, 2001; Whitmeyer and Karlstrom, 2007). In the Cananea Mining District,
 144 Paleozoic sedimentary rocks associated with the passive margin of Laurentia in southwestern
 145 North America (Stewart, 1988) are represented by quartzite and limestone that
 146 unconformably overlie the Cananea Granite (Meinert, 1982; Fig. 1). During the Triassic-
 147 Jurassic, a Cordilleran magmatic arc developed in Arizona and Sonora (Gastil et al., 1978;
 148 Tosdal et al., 1989) associated with the subduction of the Kula plate beneath the North
 149 American Plate (Brass et al., 1983). This Jurassic arc lead to the formation of volcanic and
 150 plutonic rocks ranging in age from 180 to 150 Ma (Coney and Reynolds, 1977; Anderson et
 151 al., 2005; Rodríguez-Castañeda and Anderson, 2011; Valencia-Moreno et al., 2023). In the
 152 Cananea Mining District, Meinert (1980) suggested that this period of magmatism is
 153 probably represented by the Elenita and Henrietta volcanic Formations (Valentine, 1936; Fig.
 154 1) and the El Torre Syenite pluton (Emmons, 1910; Fig. 1). The Elenita Formation is
 155 composed by a sequence of rhyolitic to andesitic tuff and flows with interbedded sandstone
 156 and quartzite (Valentine, 1936). The Henrietta Formation is composed by medium- to high-
 157 K, calc-alkaline, dacitic to rhyolitic tuff (Wodzicki, 1995) and contains clasts of rocks from
 158 the Elenita Formation (Valentine, 1936). The El Torre Syenite was described by Valentine
 159 (1936) as a pinkish-gray rock mainly composed of feldspar and hornblende \pm biotite \pm quartz
 160 and other accessory minerals.

161 After a lack of magmatic activity during the Early Cretaceous, subduction-related arc
 162 magmatism was reactivated at the end of the Early Cretaceous, associated with the
 163 subduction of the Kula-Farallon oceanic plates beneath the southwestern North American
 164 plate (Coney and Reynolds, 1977). During the Late Cretaceous-Paleogene, a northeastward

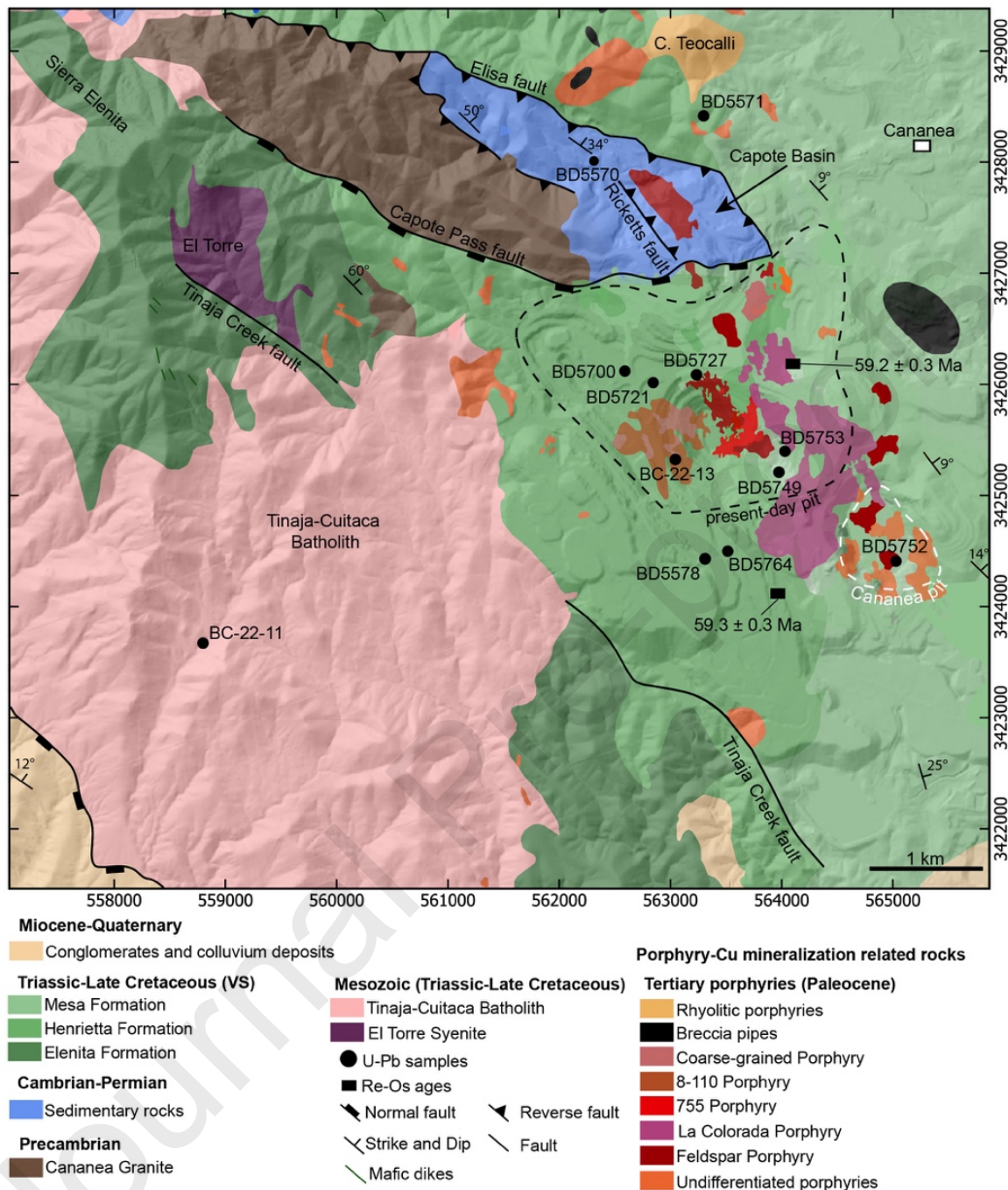
165 migration of the arc magmatism associated with a change in the subduction angle was
166 documented in southwestern North America (Coney and Reynolds, 1977; Engebretson et al.,
167 1985; Stock and Molnar, 1988). In Sonora, this period of magmatic activity has been
168 historically referred to as the “Laramide magmatic arc” because it was contemporaneous of
169 the Laramide orogeny (e.g., McDowell et al., 2001). However, Valencia-Moreno et al. (2021)
170 suggested that this term should be changed to “Cretaceous-Eocene Mexican Magmatic Arc”
171 (CEMMA) due to the characteristics of this arc in terms of tectonic style and magmatism. It
172 is during this period of magmatism, that the porphyry copper deposits of the Arizona-Sonora-
173 New Mexico cluster were emplaced (Valencia-Moreno et al., 2016; Fig. 1).

174 In the Cananea Mining District, Late Cretaceous volcanic rocks associated with the CEMMA
175 are represented by the Mariquita and Mesa Formations (Valentine, 1936; Fig. 1). The latter
176 has been dated between ~72.6 and ~65.8 Ma by the $^{40}\text{Ar}/^{39}\text{Ar}$ method (Wodzicki, 1995; Cox
177 et al., 2006). The Tinaja Diorite and the Cuitaca Granodiorite represent the plutonic part of
178 this magmatic arc (Valentine, 1936; Meinert, 1982; Wodzicki, 1995; Fig. 1). Both plutons
179 share geochemical similarities and form a composite batholith called the Tinaja-Cuitaca
180 Batholith (Valentine, 1936; Wodzicki, 1995; Fig. 1). Zircon U-Pb ages of 64 ± 3 Ma and 63.8
181 ± 1.1 Ma were obtained for the Cuitaca Granodiorite (Anderson and Silver, 1977; Del Rio-
182 Salas et al., 2013). At the end of the emplacement of the Tinaja-Cuitaca Batholith, a series
183 of quartz-feldspathic porphyry intrusions (closely related with several breccia pipes and
184 important copper-molybdenum mineralization) emplaced between ~64 and ~57 Ma (Meinert,
185 1982; Bushnell, 1988; Valencia et al., 2006; Del Rio-Salas et al., 2013 and 2017; Fig. 1).

186 After the Late Cretaceous-Early Paleogene magmatism, Sonora experienced a period of
187 tectonic quiescence from the Paleocene to the Oligocene (Wong et al., 2010). This was
188 followed by a period of intense magmatism associated with the ignimbrite “flare-up” that
189 culminated with the formation of the Sierra Madre Occidental during the Oligocene (Ferrari
190 et al., 2018). After this period, the Basin and Range continental extension began, interpreted
191 as a consequence of slab rollback or post-orogenic collapse of the crust (Coney and Harms,
192 1984; Wernicke, 1992; Sonder and Jones, 1999). In Sonora, this extension was active from
193 the Oligocene to the early Miocene (Nourse et al., 1994; McDowell et al., 1997; Gans, 1997;
194 Vega-Granillo and Calmus, 2003; Wong and Gans, 2003; Wong et al., 2010). In the Cananea
195 Mining District, the extension triggered the development of N-S trending normal faults
196 (Wodzicki, 2001; Fig. 1). It resulted in a regional eastward tilting of the Mesa Formation and
197 several breccia pipes (Perry, 1961; Meinert, 1982; Bushnell, 1988; Fig. 1) across the district,
198 as well as the formation of continental basins filled by clastic deposits intercalated with
199 basaltic flows of Oligo-Miocene age (Fig. 1).

200 **2.2. Geology of Buenavista del Cobre deposit**

201 The Buenavista del Cobre deposit is located in a tilted block controlled to the west by a west-
202 dipping normal fault (Fig. 1 and 2). This deposit is a typical porphyry Cu-Mo deposit where
203 hypogene mineralization is found within porphyry intrusions, high-grade breccia pipes, as
204 disseminated sulfides, as well as in stockwork veinlets (Perry, 1935 and 1961; Meinert, 1980;
205 Bushnell, 1988; Virtue, 1996). Post-mineralization exhumation associated with Basin and
206 Range extension promoted the development of a thick (up to 500 m) supergene chalcocite
207 blanket where the current mining activity is focused (Virtue, 1996; Ayala-Fontes, 2009).



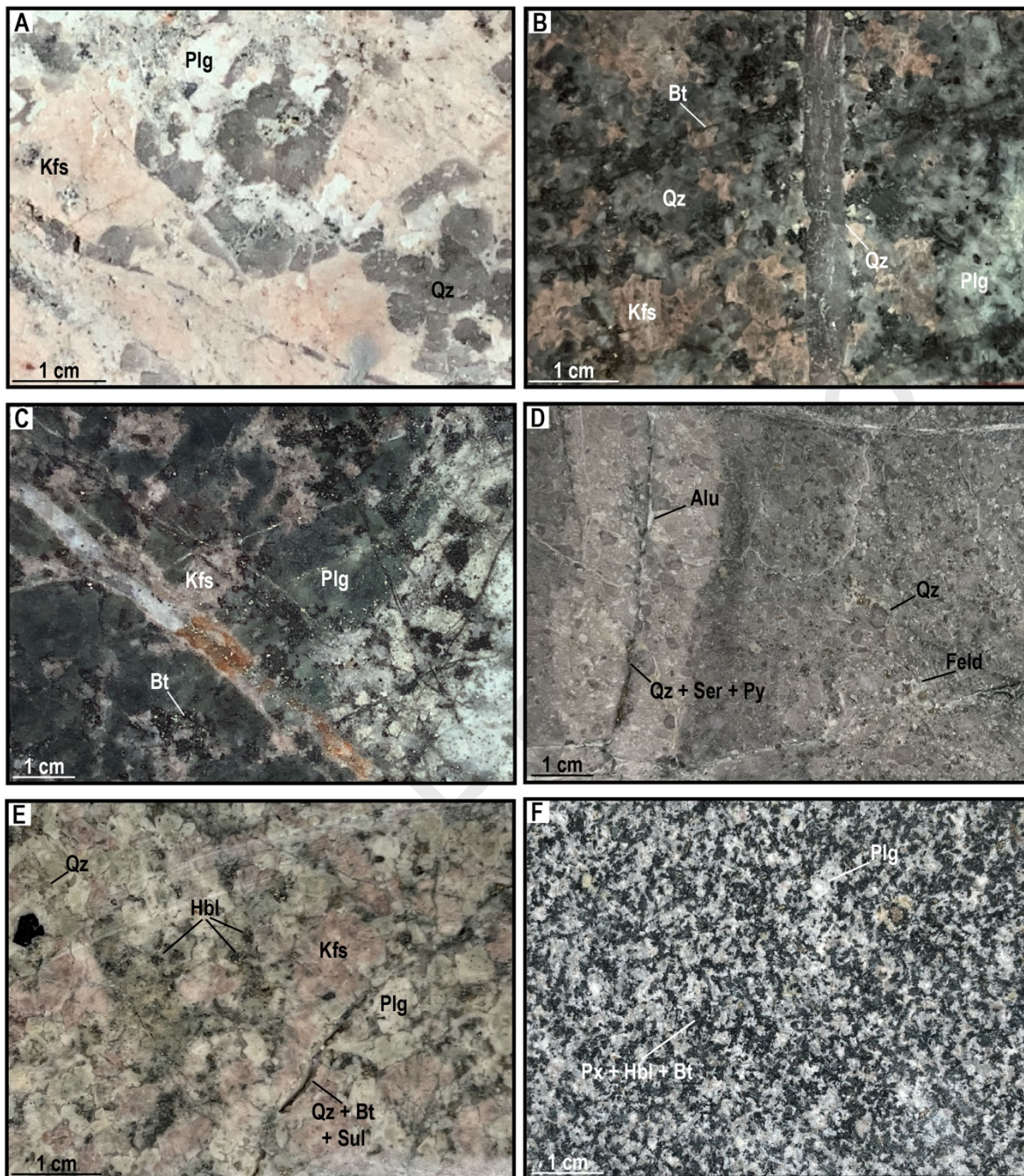
208

209 Figure 2. Geological map of the Buenavista del Cobre porphyry copper deposit, modified
 210 from Meinert (1982), Wodzicki (1995), Noguez-Alcántara (2008), Ortiz-Olvera (2022), and
 211 the geological department of Buenavista del Cobre mine.

212 In the Buenavista del Cobre deposit, the Proterozoic Cananea Granite is a coarse-grained
 213 plutonic rock that consists of centimetric K-feldspar, subhedral plagioclase and sub-rounded
 214 quartz crystals (Fig. 3A). It is unconformably overlain by the Paleozoic sediments in the
 215 northern part of the deposit (Fig. 2). This area corresponds to a horst-like structure bounded
 216 by the WNW-ESE trending Elisa and Capote Pass faults (Emmons, 1910; Valentine, 1936;

217 Meinert, 1980; Ortiz-Olvera, 2022; Fig. 2). There, the Paleozoic sedimentary rocks of the
218 Bolsa, Abrigo, Escabrosa and Martin Formations, and the Naco Group developed Zn-Cu
219 skarn mineralization (Meinert, 1980). The oldest volcanic rocks correspond to the Elenita
220 and Henrietta Formations which crop out in the western and central part of the area,
221 respectively (Fig. 2). The Henrietta Formation is considered to be younger than the Elenita
222 Formation (Valentine, 1936). The Elenita Formation was intruded by the El Torre Syenite
223 which is cut by the NW-SE trending Tinaja Creek fault at Sierra Elenita (Valentine, 1936;
224 Fig. 2). The Henrietta and Elenita Formations are in a structural contact south of the deposit
225 along the Tinaja Creek fault, which is supposed to be normal (Fig. 2). The Mesa Formation
226 is mainly exposed in the central and eastern areas of the deposit where it gently dips ($\sim 15^\circ$)
227 to the east (Fig. 2). The intrusive rocks of Tinaja-Cuitaca Batholith crop out to the northwest
228 and to the west of the current mine operation (Fig. 2).

229



230
231
232
233
234
235
236
237
238
239
240

Figure 3. Hand specimens of mineralized host rocks dated in this study. A) Cananea Granite (sample BD5753-468m). Note the selective alteration of plagioclase to sericite. B) Plutonic rock (sample BD5752-669m) with a coarse-grained texture of K-feldspar, plagioclase, quartz, and biotite. C) Coarse-grained plutonic rock (sample BD5753-627m) composed by K-feldspar, plagioclase, quartz and biotite. D) Volcanic flow of the Henrietta Formation (sample BD5571-180m) showing a porphyritic texture of anhedral quartz and feldspar phenocrysts embedded in a quartz-sericite groundmass. E) Medium-grained plutonic rock (sample BD5578-690m) composed mainly of K-feldspar, plagioclase with minor quartz, hornblende, and biotite. F) Tinaja Diorite (sample BC-22-11) showing a phaneritic texture composed mainly of plagioclase (>90%) with minor quartz, pyroxene, hornblende, and

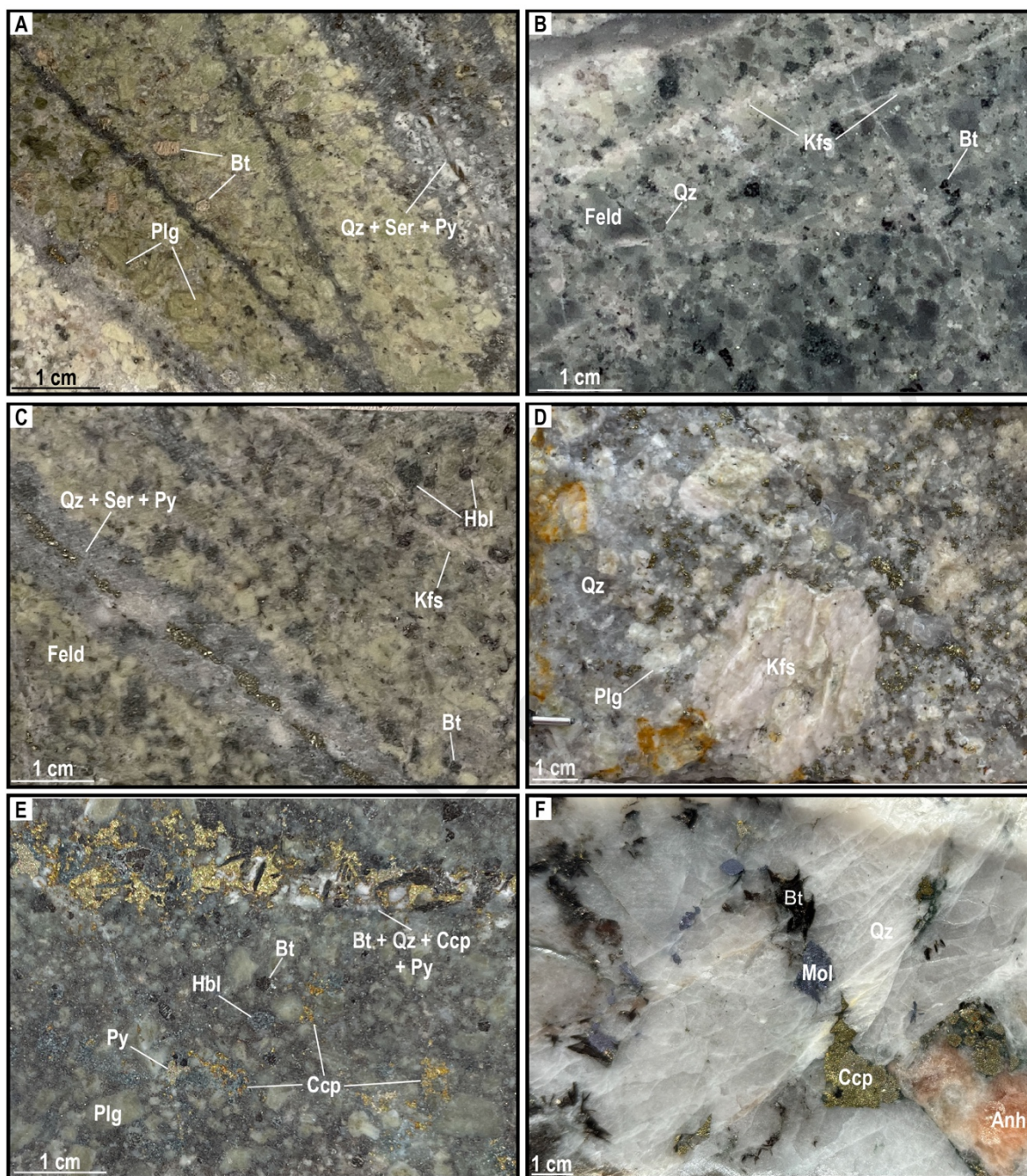
241 biotite. Qz=quartz; Feld= feldspars; Kfs= potassic feldspar; Plg= plagioclase; Px= pyroxene;
242 Hbl=hornblende; Bt=biotite; Ser= sericite; Sul=sulfides; Alu=alunite. The same
243 abbreviations will be used henceforth.

244

245 A series of ore-related porphyries intruded and hydrothermally altered and mineralized the
246 entire rock section mentioned above (Perry, 1935; Valentine, 1936; Ochoa-Landín and
247 Echávarri, 1978; Ochoa-Landín and Navarro-Meyer, 1979; Meinert, 1980; Bushnell, 1988;
248 Wodzicki, 1995; Fig. 2). The relative age of these intrusions has been established based on
249 crosscutting-relationships (Ochoa-Landín and Echávarri, 1978; Ochoa-Landín and Navarro-
250 Meyer, 1979).

251 The ore-poor Feldspar Porphyry was the first emplaced in the area and crops out in the center
252 of the present open pit and in the Capote Basin (Fig. 2), where it was emplaced along NW-
253 SE trending fractures (Ochoa-Landín and Navarro-Meyer, 1979; Fig. 2). It is a quartz-
254 monzodioritic porphyry composed of 1-2 mm feldspar phenocrysts, and 1 mm anhedral
255 quartz crystals embedded in a fine matrix of quartz-sericite (Fig. 4A). Feldspars show
256 chloritic alteration overprinted by sericitic alteration. Some biotites are brown to colorless
257 due to the sericitization. Sulfides are associated with disseminated sericite, replacing mafic
258 minerals, and occur in quartz veinlets with sericitic envelopes (Fig. 4A). According to Ochoa-
259 Landín and Navarro-Meyer (1979), this ore-poor intrusion was followed by the subsequent
260 emplacement of the La Colorada, 755 and 8-110 porphyries along N-S fractures or faults
261 (Fig. 2).

262 The ore-rich La Colorada Porphyry crops out in the eastern part of the present-day pit (Fig.
263 2) and is composed by 2-7 mm subhedral feldspar phenocrysts, and 2-3 mm sub-rounded
264 quartz crystals and biotite phenocrysts in a quartz and feldspar fine-grained matrix. Feldspars
265 from the La Colorada Porphyry show a strong silicification and thin K-feldspar veinlets (Fig.
266 4B). The high-grade La Colorada breccia pipe is genetically and spatially related to the La
267 Colorada Porphyry as it occurs at its top, where it mimics the shape of the stock (Perry, 1935
268 and 1961; Bushnell, 1988). The breccia pipe is a high-grade orebody characterized by
269 pegmatitic silicate-sulfide mineralization (6 Mt, 7% Cu and 0.8% Mo; Perry, 1935 and 1961;
270 Wodzicki, 1995). Today, this breccia no longer exists as it has been completely mined. The
271 age of the mineralization at the top of this breccia has been constrained to 59.2 ± 0.3 Ma
272 (molybdenite Re-Os dating; Barra et al., 2005; Fig. 2).



273

274 Figure 4. Hand specimens of main porphyries dated in this study. A) Feldspar Porphyry
 275 (sample BD5570-613m) showing a porphyritic texture composed of feldspars with minor
 276 quartz and biotite embedded in a fine matrix of quartz + sericite. B) La Colorada Porphyry
 277 (sample BD5753-815m) showing feldspar, quartz, and biotite phenocrysts embedded in a
 278 fine matrix of quartz and feldspar. The 755 Porphyry presents a similar texture and
 279 mineralogy. C) 8-110 Porphyry (sample BD5721-574m) showing a coarse-grained texture
 280 composed of feldspar phenocryst with quartz, biotite and hornblende. Note the quartz-
 281 sericite-pyrite veins and the thin K-feldspar veinlets. D) Coarse-grained Porphyry (sample
 282 BC-22-13) composed by quartz + K-feldspar + plagioclase. Sulfides correspond to

283 disseminated pyrite crystals. E) El Galo Porphyry (sample BD5764-826m) mineralogy
284 consists of feldspar, minor quartz, and biotite and hornblende phenocrysts. Note the
285 chalcopyrite disseminations and the biotite + quartz + sulfides vein that crosscuts the
286 porphyry. F) Potassic alteration associated with the El Galo Porphyry emplacement showing
287 a coarse-grained quartz-biotite vein associated with the precipitation of chalcopyrite,
288 molybdenite, pyrite and anhydrite. Py=pyrite; Ccp=chalcopyrite; Mol=molybdenite;
289 Anh=anhydrite.

290

291

292 The ore-rich 755 Porphyry is located in the central part of the open pit, where it crosscuts the
293 Feldspar Porphyry (Fig. 2). This intrusive consists of feldspars phenocryst and 2-3 mm quartz
294 crystals embedded in a fine silicified matrix of quartz and feldspars.

295 The ore-poor 8-110 Porphyry crops out in the western part of the present-day pit (Fig. 2). It
296 only intrudes the Henrietta Formation. It is composed by 2-7 mm feldspar and 1 mm quartz
297 phenocrysts with biotite and hornblende embedded in a fine matrix composed by quartz,
298 feldspars and sericite (Fig. 4C). In this rock, feldspars are altered to chlorite and later to
299 sericite. Hornblende has a fibrous texture and green color because of biotitization. Early thin
300 K-feldspar veinlets and late quartz-sericite-pyrite veins crosscut the porphyry (Fig. 4C).
301 Sulfides occur in disseminations and are associated with coarse-grained sericite crystals. A
302 low Cu grade tourmaline breccia is spatially related to this porphyry stock (Varela, 1972).

303 The ore-poor Coarse-grained Porphyry is often considered as the last intrusion emplaced in
304 the deposit. This porphyritic body crosscuts the 8-110 Porphyry in the western part of the
305 present-day pit (Fig. 2). It is composed of <7 mm plagioclase phenocrysts, <20 mm K-
306 feldspar (orthoclase) phenocrysts, and <5 mm sub-rounded quartz crystals (Fig. 4D). In this
307 rock, sulfides occur as disseminated pyrite crystals.

308 In this study, we report a newly discovered ore-rich porphyry (here referred to as the El Galo
309 Porphyry, Fig. 4E and F). This porphyry does not crop out at the current level of mining and
310 was identified in the drill hole BD5764 south of the present-day open pit (Fig. 2). In that area,
311 it intrudes the volcanic rocks of the Henrietta Formation (Fig. 2). It is composed by K-
312 feldspar, plagioclase, minor quartz, biotite and hornblende phenocrysts embedded in a fine
313 matrix of quartz + feldspar + biotite (Fig. 4E). In this rock, feldspars were altered by early
314 chlorite and later by sericite, and hornblende was completely replaced by small flakes of
315 biotite. The emplacement of this porphyry was accompanied by an important potassic
316 alteration characterized by the development of biotite + quartz + chalcopyrite + molybdenite
317 + pyrite + anhydrite veins (Fig. 4F).

318 Additionally, a set of sericitically altered and barren porphyry stocks consisting of large
319 rhyolitic plugs crop out north of the Buenavista del Cobre deposit (Wodzicki, 2001; Fig. 2).
320 At Cerro Teocalli, the sericite alteration has been dated in a rhyolitic porphyry at 54.2 ± 2
321 Ma (K-Ar on sericite; Wodzicki, 1995).

322 2.2.1. Alteration and mineralization

323 The alteration and mineralization patterns at Buenavista del Cobre deposit are complex.
324 Mineralization occurs in disseminated deposits with stockwork veinlets, breccia pipes,
325 breccia zones and skarn deposits (Meinert, 1980; Bushnell, 1988; Wodzicki, 1995; Virtue,
326 1996). For practical purposes, the alteration and mineralization processes associated with Cu-
327 Mo mineralization has been divided into early and late alteration and mineralization, based
328 on cross-cutting relationships (Bushnell, 1988). The alteration and mineralization related to
329 the development of skarn deposits is beyond the scope of this study, but the reader is referred
330 to Meinert (1980) for a detailed description.

331 Early alteration and the precipitation of disseminated sulfides have been interpreted as being
332 associated with the emplacement of the La Colorada Porphyry and formation of the La
333 Colorada breccia pipe (Bushnell, 1988 and references therein). This alteration consists of thin
334 veinlets of quartz, K-feldspar and sulfides in conjunction with metasomatic K-feldspar and
335 biotite (Bushnell, 1988). At La Colorada breccia pipe, a potassic alteration consisting of
336 quartz + K-feldspar + biotite pegmatitic zones with Cu(Fe) sulfides, and molybdenite has
337 been described (Wodzicki, 1995). The age of this alteration was constrained by K/Ar on
338 phlogopite at 59.9 ± 2.1 Ma (Damon and Mauger, 1966) and 58.5 ± 2.1 Ma (Varela, 1972).
339 Moreover, widespread propylitic alteration characterized by partial replacement of
340 ferromagnesian minerals by actinolite and chlorite \pm sphene \pm rutile, and alteration of
341 plagioclase to sericite \pm clays and epidote is probably contemporaneous with the early
342 mineralization (Virtue, 1996; Wodzicki, 1995). This propylitic alteration is well developed
343 at the Tinaja and El Torre plutons, to the west of the study area (Wodzicki, 1995).

344 Late alteration has been interpreted to correspond to quartz-sericite (phyllic) hydrothermal
345 alteration. This alteration type is the dominant alteration at the Buenavista del Cobre deposit
346 and extends to a depth of ~ 1 km (Schwartz, 1947; Meinert, 1980; Bushnell, 1988; Virtue,
347 1996). At shallow levels, this alteration overprints the early alteration mineral assemblages
348 described above. The associated hypogene mineralization occurs mainly disseminated within
349 the volcanic host rocks and within the porphyries, and has been dated by Re-Os on
350 molybdenite at 59.3 ± 0.3 Ma in a phyllic-altered quartz-feldspar porphyry with disseminated
351 chalcopyrite and molybdenite (Barra et al., 2005). The intense and pervasive phyllic
352 alteration is characterized by the replacement of feldspars by sericite and of the mafic
353 minerals by sericite \pm pyrite \pm chalcopyrite (Wodzicki, 1995).

354 A late argillic alteration is also reported at the Buenavista del Cobre deposit. It consists of
355 fine-grained clay (kaolinite), quartz, and alunite (Wodzicki, 1995; Virtue, 1996). It was
356 locally documented in the upper levels of La Colorada Porphyry where the sericitic alteration
357 is crosscut by alunite veinlets (Perry, 1961; Wodzicki, 1995), and in some areas of the
358 disseminated mineralization. An hypogene origin for this alteration has been proposed
359 (Wodzicki, 1995; Bushnell, 1988). However, host rock interaction with supergene acid fluids
360 may be the origin of some argillic alteration zones and alunite veinlets (Bushnell, 1988;
361 Virtue, 1996).

362 A thick supergene alteration profile characterizes the Buenavista del Cobre deposit and
363 makes it economically significant. It consists, from top to bottom, of a leached capping oxide
364 zone, a secondary copper sulfide enriched zone, a partially enriched zone (mixture of
365 hypogene and supergene mineralization), and a primary mineralization zone (Virtue, 1996).

366 The supergene enrichment mineralogy mainly consists of chalcocite and covellite replacing
367 and coating hypogene Cu sulfides in disseminations and veinlets (Virtue, 1996).

368

369 **2.2.2. Structure**

370 Several major faulting episodes have been reported in the Buenavista del Cobre deposit. An
371 early episode is represented by a group of steeply dipping WNW-ESE trending faults
372 corresponding to the Elisa, Capote Pass, Tinaja Creek, and Ricketts faults (Emmons, 1910;
373 Valentine, 1936; Fig. 2). In particular, the Elisa and Capote Pass faults bound the Cananea
374 Granite and the Paleozoic sedimentary rocks in the Capote Basin (Fig. 2). The NNW-SSE
375 Ricketts reverse fault cuts part of the Paleozoic sequence (Ortiz-Olvera, 2022; Fig. 2). The
376 Tinaja Creek fault controls the southwestern border of the El Torre Syenite pluton and
377 separates the Elenita Formation from the Henrietta Formation in the western part of the
378 deposit (Fig. 2). The interpretation of the kinematics of these faults remains poorly
379 documented. Ortiz-Olvera (2022) proposed that the Elisa and Ricketts faults are reverse faults
380 that were active between 67 and 64 Ma during the Laramide compression. In addition, a
381 normal displacement sense of faulting has been proposed for the Capote Pass fault, which
382 was probably active in the Oligo-Miocene during the Basin and Range extension (Ortiz-
383 Olvera, 2022).

384 A late episode of faulting is represented by N-S to NW-SE trending normal faults that cut all
385 the rocks in the deposit. In particular, the main faults belonging to this family occur at the
386 westernmost border of the study area (Fig. 2) and control the tilting of the structural block
387 where the deposit occurs. This post-mineralization faulting consists of high-angle normal
388 faults associated with the Basin and Range extension and influenced the oxidation and
389 supergene enrichment in the Buenavista del Cobre deposit (Bushnell, 1988; Wodzicki, 1995;
390 Virtue, 1996).

391

392 **3. Methodology and analytical techniques**

393 Samples of texturally and compositionally different porphyritic and intrusive host rocks were
394 taken either from drill holes or outcrops at different locations in the Buenavista del Cobre
395 deposit (Fig. 2). A complete petrographic description of the analyzed samples can be found
396 in the Supplementary material (S1). Four samples from the igneous host rocks (Fig. 2 and 3),
397 one sample from the precursor batholith (Tinaja Diorite; Fig. 2 and 3F) and five different
398 samples from the main porphyry intrusions were collected for zircon U-Pb geochronology
399 (Fig. 2 and 4). Concerning apatite trace elements compositions and U-Pb geochronology, two
400 samples from the igneous host rocks and six samples from ore-related porphyries were
401 analyzed. In order to compare the apatite geochemical characteristics of the ore-rich and ore-
402 poor porphyry intrusions at Buenavista del Cobre deposit, the main porphyries (Fig. 4) were
403 sampled based on their metal contribution and were divided into two groups: (1) ore-rich
404 porphyries represented by La Colorada, 755 and El Galo porphyries samples, and (2) ore-
405 poor porphyries represented by the 8-110 and the Coarse-grained porphyries samples.

406 After crushing and sieving, magnetic and heavy mineral separation techniques were used to
 407 isolate zircon and apatite crystals. Crystals were then hand-picked from the heavy fraction
 408 under a binocular microscope. Around 50-100 apatite and zircon grains for each sample were
 409 embedded in an epoxy resin and polished to expose their inner part.

410 LA-ICP-MS U-Pb dating was performed on all the collected samples. All analyses were
 411 performed at the GeOHeLiS Platform, University of Rennes, France, using an ESI
 412 NWR193UC Excimer laser coupled to an Agilent 7700x Q-ICP-MS. The analytical
 413 procedure and instrument operating conditions are detailed in the Supplementary file S2.
 414 Zircon grains were imaged by cathodoluminescence and then analyzed with a 25 μm round
 415 spot (Supplementary material S3), with a repetition rate of 4 Hz and a fluence of 6 J/cm^2 .
 416 The GJ-1 zircon was used as a primary standard (Jackson et al., 2004), while the Plesovice
 417 (Sláma et al., 2008) and Fish Canyon Tuff (Boehnke and Harrison, 2014) zircon reference
 418 materials were used for quality control. Additional information on the analytical protocol can
 419 be found in Nosenzo et al. (2022). Apatite U-Pb and trace elements concentration data were
 420 acquired using apatite fission track protocol of Cogné et al. (2020) on inclusion free-grains,
 421 using a 30 μm round spot with a 5 Hz repetition rate and 4 J/cm^2 fluence. For U-Pb standard
 422 bracketing, the Madagascar apatite (Thomson et al., 2012) was used as a primary standard,
 423 the McClure apatite (Schoene and Bowring, 2006) and Durango apatite (McDowell et al.,
 424 2005) were employed as quality control material.

425 Data reduction was carried out with the Iolite data reduction scheme U-Pb Geochronology
 426 (Paton et al. 2010) for zircon, and the data reduction scheme Vizual-Age_UcomPbine (Chew
 427 et al. 2014) for apatite. Concordia ages and diagrams were generated using IsoplotR
 428 (Vermeesch, 2018). In the case of zircon U-Pb data, a threshold of $\pm 2\%$ of concordance of
 429 a single grain was used to select zircon grains for concordia date calculations. Concordia
 430 dates are quoted with two uncertainties, without and with systematic uncertainties propagated
 431 (Horstwood et al., 2016; Table 1).

432 Apatite Cl (wt %) concentrations were calculated using the protocol of Chew et al. (2014)
 433 with McClure apatite as a low-Cl standard and a synthetic Cl-apatite (Klemme et al., 2013)
 434 as a high-Cl standard. Trace element data were reduced using the TraceElement DRS, with
 435 NIST 612 as external standard (Jochum et al., 2011) and ^{43}Ca as internal standard with a
 436 value 39.36% for apatite. McClure apatite are used as quality control material (Cogné et al.,
 437 2024). Concentration calculated were then normalised to chondrite values (Barrat et al.,
 438 2012). Eu and Ce anomalies were calculated according to Lodders (2010) with $\text{Eu}/\text{Eu}^* =$
 439 $\text{Eu}_{\text{CN}} \cdot (\text{Sm}_{\text{CN}} \cdot \text{Gd}_{\text{CN}})^{-0.5}$ and $\text{Ce}/\text{Ce}^* = \text{Ce}_{\text{CN}} \cdot (\text{La}_{\text{CN}} \cdot \text{Pr}_{\text{CN}})^{-0.5}$.

440

441 4. Results

442 4.1. Petrology of the El Galo Porphyry

443 In this study, we report a newly discovered porphyry (here referred as El Galo Porphyry)
 444 intersected by exploration drilling. This porphyry does not crop out at the current level of
 445 mining and was identified in the drill hole BD5764 to the south of the present-day open pit

446 where it intrudes and mineralizes the volcanic rocks of the Henrietta Formation (Fig. 2). It is
447 composed by K-feldspar, plagioclase, minor quartz, biotite and hornblende phenocrysts
448 embedded in a fine matrix of quartz + feldspar + biotite (Fig. 4E). This porphyry is spatially
449 associated with a potassic alteration zone expressed as massive coarse-grained hydrothermal
450 veinlets of biotite + quartz + chalcopyrite + pyrite + molybdenite + anhydrite, and
451 disseminations of chalcopyrite, molybdenite and pyrite (Fig. 4F). Based on these
452 observations, we classify the El Galo Porphyry as an ore-rich porphyry such as the La
453 Colorada and 755 porphyries.

454

Journal Pre-proofs

Table 1. Zircon and apatite U-Pb dates for the Buenavista del Cobre host rocks and main porphyries. Coordinates in WGS84, UTM zone 12.

Sample ID	Rock type	Coordinates			U-Pb date (Ma)
		UTM (N)	UTM (E)	Elevation (m)	
Zircon U-Pb dating					
BD5753-468 m	Intrusive host rock	3425398	564031	1107	1421 ± 14/18
BD5752-669 m	Intrusive host rock	3424409	565029	889	186.9 ± 1.3/3.1
BD5571-180 m	Henrietta Formation	3428416	563299	1594	186.8 ± 1.1/3.0
BD5578-690 m	Intrusive host rock	3424429	563312	1094	176.3 ± 1.1/2.9
BC-22-11	Tinaja Diorite	3423671	558799	1704	73.8 ± 0.6/1.3
BD5570-613 m	Feldspar Porphyry	3428010	562314	1175	59.7 ± 0.5/1.1
BD5753-815 m	La Colorada Porphyry	3425398	564031	760	58.9 ± 0.5/1.0
BD5749-606 m	755 Porphyry	3425209	563977	969	57.5 ± 0.2/0.9

BD5721-574 m	8-110 Porphyry	3426015	562846	895	56.5 ± 0.3/0.9
BD5764-826 m	El Galo Porphyry	3424498	563516	948	56.1 ± 0.2/0.9

Apatite U-Pb dating

BD5753-627 m	Intrusive host rock	3425398	564031	948	56.7 ± 4.6
BD5578-690 m	Intrusive host rock	3424429	563312	1094	54 ± 10
BD5753-815 m	La Colorada Porphyry	3425398	564031	760	59.2 ± 2.2
BD5749-606 m	755 Porphyry	3425209	563977	969	58.3 ± 3.1
BD5727-547 m	8-110 Porphyry	3426084	563237	833	56.8 ± 2.6
BD5700-711 m	8-110 Porphyry	3426116	562591	827	56.8 ± 1.9
BD5721-574 m	8-110 Porphyry	3426015	562846	895	56.0 ± 4.6
BD5764-826 m	El Galo Porphyry	3424498	563516	948	57.0 ± 8.2

455

456

Journal Pre-proofs

4.2. Zircon U-Pb dating

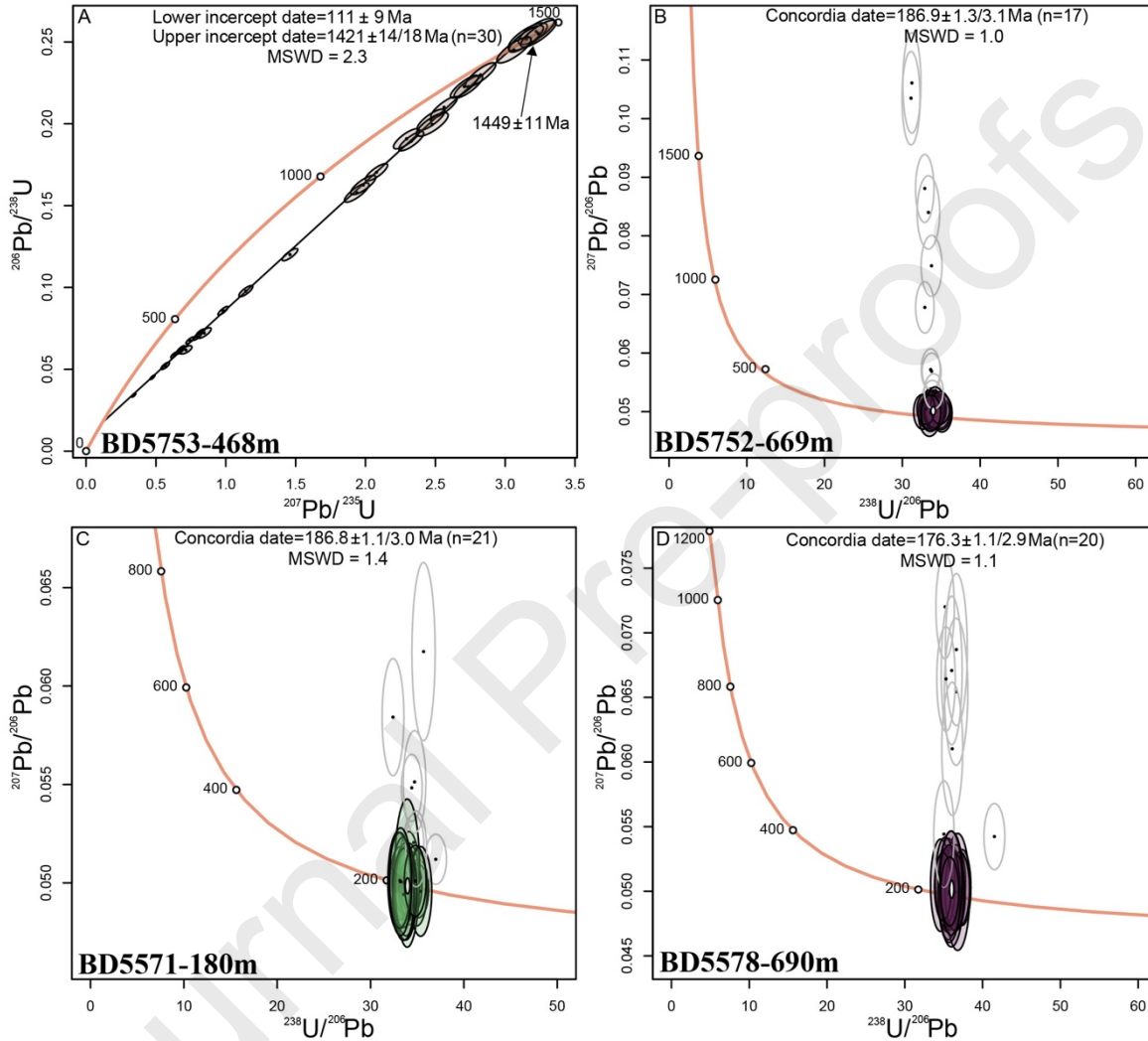
457
458 Four new zircon U-Pb dates (Table 1) have been obtained from different igneous host rocks
459 at Buenavista del Cobre deposit (Wetherill and Tera-Wasserburg concordia plots are reported
460 in Figure 5 and data in Supplementary Table S4). Zircon grains from sample BD5753-468m,
461 supposedly belonging to the Cananea Granite (Fig. 3A), are predominantly prismatic and
462 elongated (186-350 μm in size) and show oscillatory or patchy zoning (e.g., G15 and G13,
463 respectively; S3 Fig. 1). The analyzed zircon grains show high U (186-2525 ppm) and Pb
464 (330-1012 ppm) contents with Th/U ratios ranging from 0.11 to 0.31. Thirty analyses
465 performed in zircon rims (S3 Fig. 1) define a discordia line with an upper intercept date of
466 $1421 \pm 14/18$ Ma and a lower intercept date of $111 \pm 9/9$ Ma ($n=30$, MSWD=2.3; Fig. 5A).
467 Five analyzed zircon grains yield a concordia date of 1449 ± 11 Ma ($n=5$, MSWD=1.1; Fig.
468 5A).

469 We also analyzed zircons from sample BD5752-669m, a coarse-grained intrusive host rock
470 with K-feldspar, plagioclase, quartz and biotite phenocrysts (Fig. 3B). In this rock,
471 plagioclase is altered to chlorite and mafic minerals are replaced by small grains of biotite.
472 Thin veinlets of biotite crosscut the rock and are cut by late quartz-sericite veins. Sulfides are
473 associated with biotite and quartz-sericite veins, and also occur as disseminations. Zircon
474 crystals from this rock are stubby, euhedral to subhedral (166 to 373 μm in size), mostly with
475 a concentric oscillatory zoning (S3 Fig. 1) and less commonly with patchy zoning (e.g., G23;
476 S3 Fig. 1). They can also present inherited cores (e.g., G22; S3 Fig. 1). All the analyses were
477 performed in the zircon rims (S3 Fig. 1) and show variable U (310-1248 ppm) and Pb (65-
478 2086 ppm) contents with Th/U ratios ranging from 0.23 to 0.34. Seventeen zircon analyses
479 yield a concordia date of $186.9 \pm 1.3/3.1$ Ma ($n=17$, MSWD=1.0; Fig. 5B). The remaining
480 analyses are discordant because of the presence of a non-negligible and variable amount of
481 common Pb ($f_{206\text{c}} > 0.2\%$, Supplementary Table S4).

482 Sample BD5571-180m corresponds to a porphyritic volcanic rock of the Henrietta Formation
483 conformed by anhedral quartz and feldspar phenocrysts embedded in a quartz-sericite
484 groundmass (Fig. 3D). Quartz-pyrite veinlets with sericite envelopes are common in this
485 sample of the Henrietta Formation, it has to be noted that thin supergene white alunite
486 veinlets tapped the quartz-sericite veinlets to precipitate. Zircons from this sample are
487 prismatic (240-333 μm in size) with concentric oscillatory zoning and, more rarely, patchy
488 zoning (e.g., G24; S3 Fig. 1). All the analyses were performed in the zircon rims (S3 Fig. 1).
489 They show high U (278-4850 ppm) and Pb (57-1828 ppm) contents with Th/U ratios ranging
490 from 0.18 to 0.83. Twenty-one zircon analyses yield a concordia date of $186.8 \pm 1.1/3.0$ Ma
491 ($n=21$, MSWD=1.4; Fig. 5C). The remaining data are discordant due to the presence of
492 common Pb in the crystals lattice ($f_{206\text{c}} > 0.2\%$, Supplementary Table S4).

493 Finally, sample BD5578-690m corresponds to a medium-grained plutonic host rock
494 composed of K-feldspar and plagioclase with minor quartz, hornblende and biotite (Fig. 3E).
495 In this rock, hornblende is often replaced by small grains of biotite, and selective
496 chloritization of plagioclase is observed. Thin veinlets of quartz + biotite + sulfides crosscut
497 the rock (Fig. 3E). Zircon crystals from this sample are prismatic (166-369 μm in size) with
498 oscillatory (e.g., G5; S3 Fig. 1) and patchy zoning (e.g., G26, G7 and G10; S3 Fig. 1). They
499 can sometimes display some inherited cores (e.g., G23; S3 Fig. 1). Zircon grains have low U

500 (30-121 ppm) and Pb (18-225 ppm) contents with Th/U ratios ranging from 0.20 to 0.33.
 501 Twenty analyses performed in the zircon rims (S3 Fig. 1) yield a concordia date of $176.3 \pm$
 502 $1.1/2.9$ Ma ($n=20$, MSWD=1.1; Fig. 5D). Here again, the remaining data are discordant
 503 because of the presence of a non-negligible amount of common Pb ($f_{206c} > 0.6\%$,
 504 Supplementary Table S4).



505

506 Figure 5. Wetherill and Tera-Wasserburg concordia plots of zircon U-Pb analysis of the
 507 intrusive host rocks of the Buenavista del Cobre deposit. Concordia dates are reported with
 508 two different uncertainties separated by a dash bar (/): the first one without propagating the
 509 systematic uncertainties and the second after proper propagation (Horstwood et al., 2016).

510

511 Six new zircon U-Pb dates (Table 1) are reported for the precursor batholith and ore-related
 512 porphyry rocks (Tera-Wasserburg concordia plots are reported in Figure 6 and data in
 513 Supplementary Table S4). Zircon grains from the Tinaja Diorite (sample BC-22-11; Fig. 2)
 514 are stubby, euhedral to subhedral (266-340 μm in size) with distinct morphology and texture
 515 when compared to the zircon crystals from the porphyry rocks (S3 Fig. 2). Indeed, the crystals

516 commonly exhibit a zoning marked by wide dark-CL zones and narrow bright-CL zones (S3
517 Fig. 2) and, less commonly, are characterized by the presence of concentric oscillatory (eg.,
518 G5; S3 Fig. 2) or patchy zoning (G7; S3 Fig. 2). All the analyses were performed in zircon
519 outer parts (S3 Fig. 2) and show variable U (445-2448 ppm) and Pb (34-372 ppm) contents
520 with Th/U ratios ranging from 0.13 to 0.50. Twenty-three U-Pb zircon analyses yield a
521 concordia date of $73.8 \pm 0.6/1.3$ Ma ($n=23$, MSWD=2.0; Fig. 6A). The remaining analyses
522 plot in a discordant position owing for the presence of a non-negligible amount of common
523 Pb (f206c up to 18%, Supplementary Table S4).

524 Five zircon U-Pb dates have been obtained from the main porphyritic intrusions at Buenavista
525 del Cobre deposit (Table 1; Fig. 6), which are compositionally and texturally different (Fig.
526 4). In general, zircon grains from porphyry rocks have needle-like shapes (80-380 μm in size)
527 with concentric oscillatory growth zoning (S3 Fig. 2), which is typical of magmatic zircon
528 that crystallized in fast-cooling intrusions (Corfu, 2003; Nathwani et al., 2023). Zircon grains
529 from sample BD5570-613m collected from the NW-SE trending Feldspar Porphyry (Fig. 2)
530 show variable U (510-1824 ppm) and Pb (35-333 ppm) contents with Th/U ratios ranging
531 from 0.23 to 0.71. Fifteen zircon U-Pb analyses performed either in the inner or the outer
532 parts of the grains (S3 Fig. 2) yield a concordia date of $59.7 \pm 0.5/1.1$ Ma ($n=15$, MSWD=0.4;
533 Fig. 6B). A second group of four concordant analyses yield a concordia date of $65.1 \pm 1.0/1.5$
534 Ma ($n=4$, MSWD=0.4; Fig. 6B), while one grain is concordant at ca. 174 Ma (Fig. 6B). The
535 remaining data are discordant due to the presence of common Pb (f206c>0.4%,
536 Supplementary Table S4).

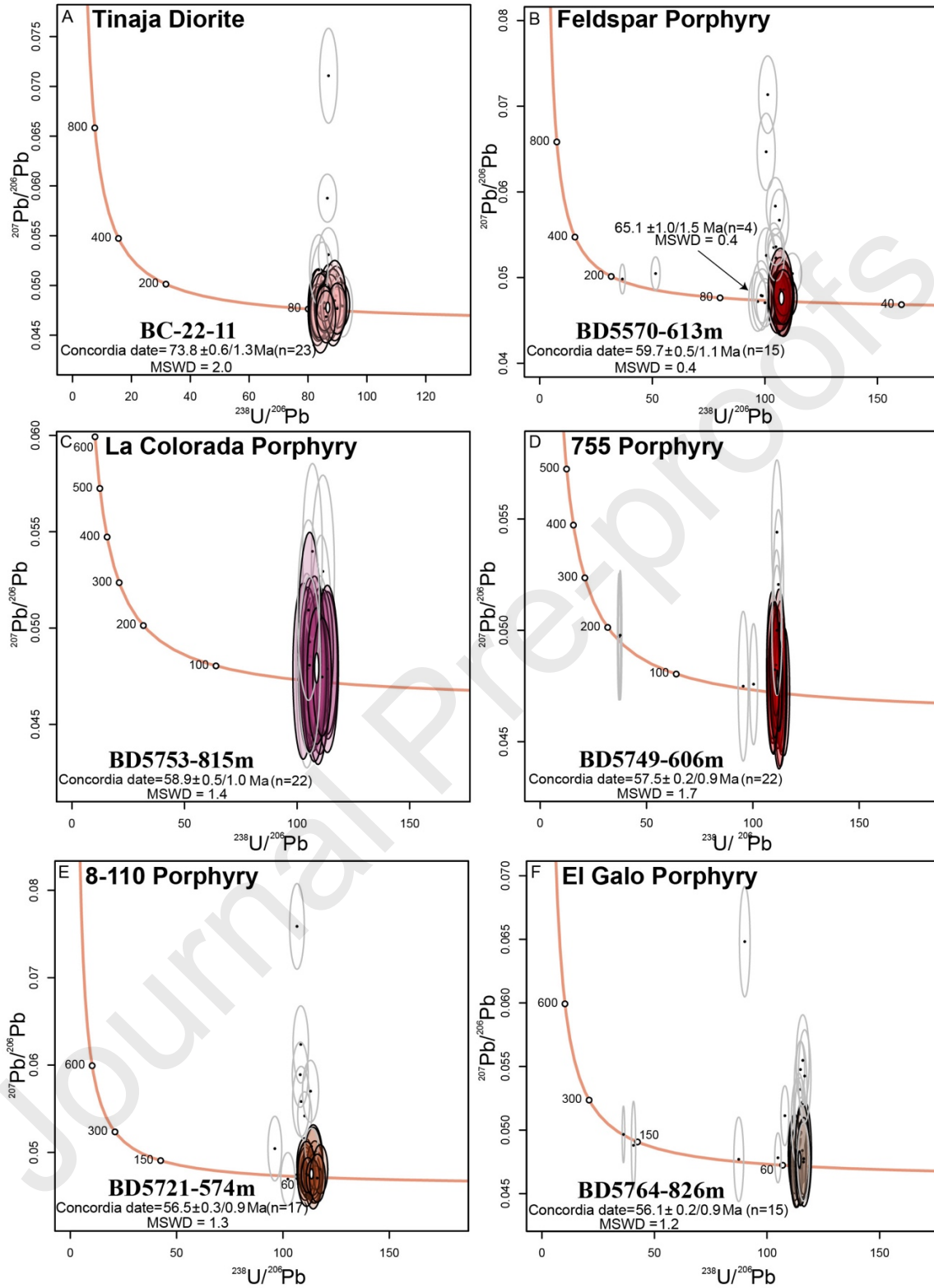
537 Zircon crystals from the La Colorada Porphyry (sample BD5753-815m) show variable U
538 (175-1132 ppm) and Pb (13-329 ppm) contents and Th/U ratios ranging from 0.15 to 0.35.
539 Twenty-two analyses performed in zircon outer parts (S3 Fig. 2) yield a concordia date of
540 $58.9 \pm 0.5/1.0$ Ma ($n=22$, MSWD=1.4; Fig. 6C). The remaining data are slightly discordant
541 because of the presence of a slight amount of common Pb (f206c>0.1%, Supplementary
542 Table S4).

543 Zircon grains from the 755 Porphyry (sample BD5749-606m) show variable U (250-1434
544 ppm) and Pb (16-125 ppm) contents, and Th/U ratios ranging from 0.18 to 0.36. Twenty-two
545 analyses performed in zircon outer parts (S3 Fig. 2) yield a concordia date of $57.5 \pm 0.2/0.9$
546 Ma ($n=22$, MSWD=1.7; Fig. 6D). Two concordant analyses yield dates of around ~ 170 Ma
547 (Fig. 6D) while two others yield dates around ~ 65 Ma (Fig. 6D). The remaining analyses are
548 slightly discordant due to the presence of a slight amount of common Pb in the crystal lattice
549 (f206c>0.4%, Supplementary Table S4).

550 Zircon crystals from the 8-110 Porphyry (sample BD5721-574m) show high U (138-3593
551 ppm) and Pb (22-520 ppm) contents with Th/U ratios ranging from 0.11 to 0.49. Seventeen
552 zircon U-Pb analyses performed in the inner and outer parts of the crystals (S3 Fig. 2) yield
553 a concordia date of $56.5 \pm 0.3/0.9$ Ma ($n=17$, MSWD=1.3; Fig. 6E). One older ~ 63 Myr old
554 zircon was analyzed (Fig. 6E). The remaining analyses are discordant because of the presence
555 of common Pb in these grains (f206c up to 22.6%, Supplementary Table S4).

556 Zircon grains from the newly discovered El Galo Porphyry (sample BD5764-826m) show
557 variable U (93-1340 ppm) and Pb (23-114 ppm) contents with Th/U ratios ranging from 0.16

558 to 0.42. Fifteen analyses were performed either in the inner or outer parts of the grains (S3
559 Fig. 2) and yield a concordia date of $56.1 \pm 0.2/0.9$ Ma ($n=15$, $MSWD=1.2$; Fig. 6F). Four
560 concordant zircons yield dates of ~ 175 Ma, ~ 156 Ma, ~ 73 Ma and ~ 61 Ma, respectively (Fig.
561 6F). The remaining analyses have $\epsilon_{206} > 0.3\%$ and are therefore discordant (Supplementary
562 Table S4). We also sampled the Coarse-grained Porphyry which crosscuts the 8-110
563 Porphyry in the western part of the present-day pit (sample BC-22-13, Fig. 2 and 4D).
564 However, we did not find any apatite or zircon, probably because it displays strong acidic
565 hydrothermal alteration that could be responsible for the dissolution of the apatite and zircon
566 grains. Probably for the same reason, we did not find apatite crystals in the Feldspar
567 Porphyry.



568

569 Figure 6. Tera-Wasserburg concordia plots of zircon U-Pb analysis of the precursor batholith
 570 and main porphyries of the Buenavista del Cobre deposit. Colorless grains in the plot

571 represent discordant ages and zircon inherited ages that were not considered in the calculation
572 of the concordia date.

573

574 **4.3. Apatite U-Pb dating**

575 Two new apatite U-Pb dates (Table 1) are reported for intrusive host rocks of the Buenavista
576 del Cobre deposit (Tera-Wasserburg plots with apatite U-Pb lower intercept dates are
577 reported in Figure 7 and data in Supplementary Table S5). Apatite grains from sample
578 BD5753-627m (Fig. 3C) are subhedral to anhedral with tabular and prismatic shapes (284-
579 721 μm in size). For this sample, 37 apatite grains were analyzed. They are characterized by
580 high U (9 to 43 ppm) and homogeneous Pb (3 to 8 ppm) contents. In a Tera-Wasserburg
581 diagram, they plot in a discordant position and yield a lower intercept U-Pb date of $56.7 \pm$
582 4.6 Ma ($n=37$, MSWD=1.1; Fig. 7A) with an initial common Pb value of $(^{207}\text{Pb}/^{206}\text{Pb})_c = 0.83$
583 ± 0.02 . For sample BD5578-690m, 24 analyses were performed. Apatite grains are mostly
584 subhedral to anhedral with stubby, tabular and prismatic shapes (291-642 μm in size). They
585 are characterized by fairly homogeneous U (3 to 34 ppm) and Pb (4 to 9 ppm) contents with
586 variable Th/U ratios ranging from 0.05 to 1.93. Plotted in a Tera-Wasserburg diagram (Fig.
587 7B), they are all discordant and yield a lower intercept U-Pb date of 54.0 ± 10 Ma ($n=24$,
588 MSWD=0.8; Fig. 7B) with a $(^{207}\text{Pb}/^{206}\text{Pb})_c = 0.83 \pm 0.02$.

589 Apatite analyses from six samples from the ore-related porphyries yielded lower intercept
590 apatite U-Pb dates ranging from 59.2 ± 2.2 to 56.0 ± 4.6 Ma (Table 1 and Fig. 7; apatite U-
591 Pb data are available in Supplementary Table S5). In general, apatite grains from porphyry
592 rocks are commonly subhedral to anhedral (225-927 μm in size) with broken-off tips and less
593 commonly stubby and prismatic in shape. In the La Colorada Porphyry (sample BD5753-
594 815m) 27 apatites were analyzed. They have variable U (1-123 ppm) and more consistent Pb
595 (4-9 ppm) contents with Th/U ratios ranging from 0.17 to 1.35. All the apatite U-Pb analyses
596 plot in a discordant position and yield a lower intercept date of 59.2 ± 2.2 Ma ($n=27$,
597 MSWD=1.2; Fig. 7C) with an initial common lead composition value of $(^{207}\text{Pb}/^{206}\text{Pb})_c = 0.84$
598 ± 0.02 .

599 Apatite grains of the 755 Porphyry (sample BD5749-606m) yield variable U (1-85 ppm) and
600 more consistent Pb (2-9 ppm) contents with Th/U ratios ranging from 0.16 to 0.96. Twenty-
601 two analyses define a discordia line with a lower intercept U-Pb date of 58.3 ± 3.1 Ma ($n=22$,
602 MSWD=0.7; Fig. 7D) with $(^{207}\text{Pb}/^{206}\text{Pb})_c = 0.86 \pm 0.02$.

603 The apatite grains from three samples from the 8-110 Porphyry yielded similar lower
604 intercept apatite U-Pb dates (Fig. 7). Twenty-eight apatite grains were analyzed from sample
605 BD5727-547m. They have variable U (13-90 ppm) and Pb (6-17 ppm) contents with Th/U
606 ratios ranging from 0.08 to 0.95. In the Tera-Wasserburg diagram, all the analyses plot in a
607 discordant position and yield a lower intercept date of 56.8 ± 2.6 Ma ($n=28$, MSWD=1.4;
608 Fig. 7E) with $(^{207}\text{Pb}/^{206}\text{Pb})_c = 0.84 \pm 0.02$. Sample BD5700-711m have apatite grains with
609 variable U (14-118 ppm) and Pb (4-7 ppm) contents with Th/U ratios ranging from 0.08 to
610 2.61. Thirty-seven analyses define a discordia line with a lower intercept date of 56.8 ± 1.9
611 Ma ($n=37$, MSWD=0.8; Fig. 7F) with $(^{207}\text{Pb}/^{206}\text{Pb})_c = 0.83 \pm 0.02$. Apatite crystals from

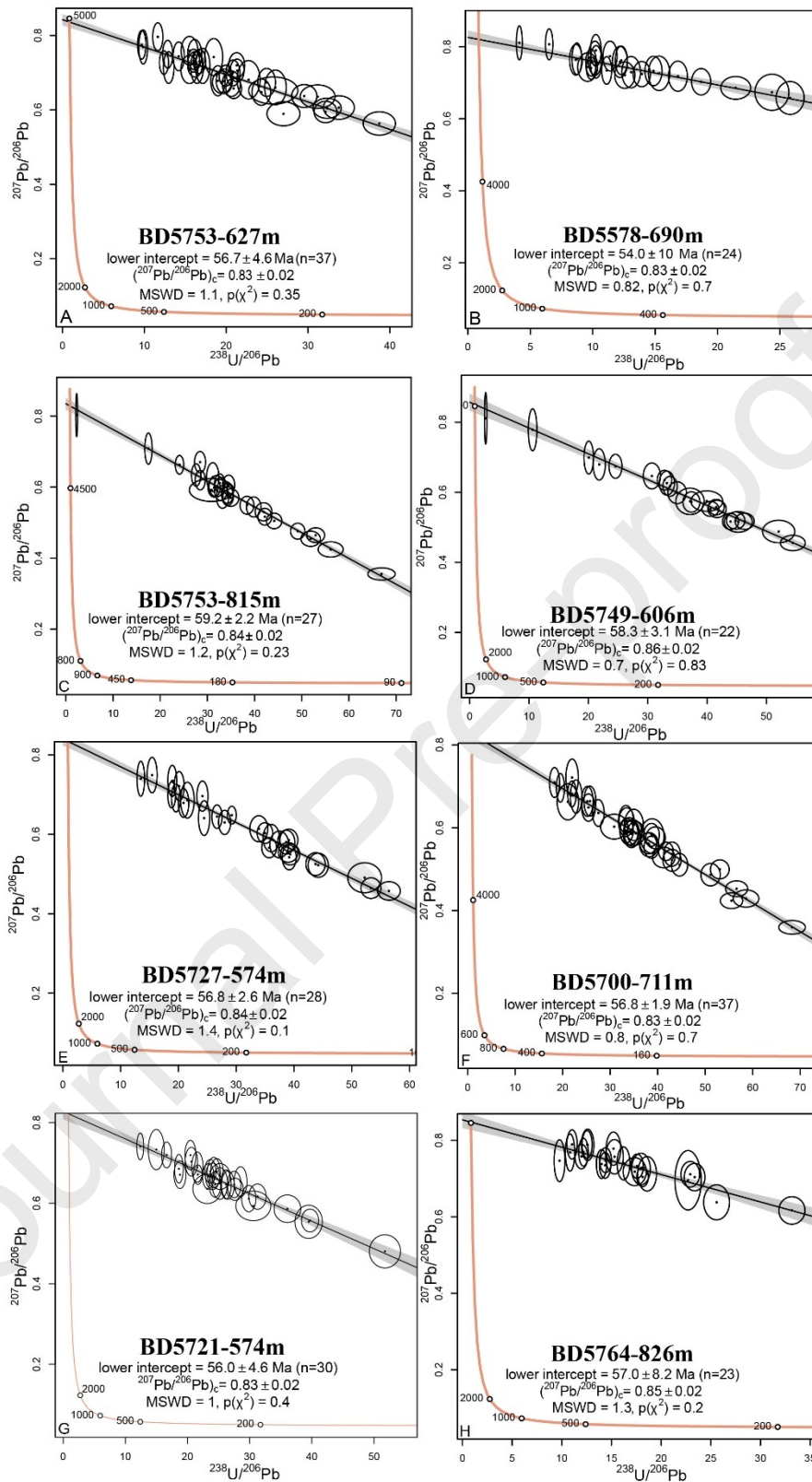
612 sample BD5721-574m have variable U (12-77 ppm) and Pb (3-9 ppm) contents with Th/U
613 ratios ranging from 0.36 to 1.27. Thirty analyses yielded a lower intercept date of and $56.0 \pm$
614 4.6 Ma ($n=30$, MSWD=1.0; Fig. 7G) with $(^{207}\text{Pb}/^{206}\text{Pb})_c = 0.83 \pm 0.02$.

615 Finally, the apatite grains from El Galo Porphyry (sample BD5764-826m) have variable U
616 (8-41 ppm) and consistent Pb (4-11 ppm) contents with Th/U ratios ranging from 0.15 to
617 4.44. A total of 23 analyses yielded a lower intercept U-Pb date of 57.0 ± 8.2 Ma
618 (MSWD=1.3; Fig. 7H) with $(^{207}\text{Pb}/^{206}\text{Pb})_c = 0.85 \pm 0.02$.

619

620

621



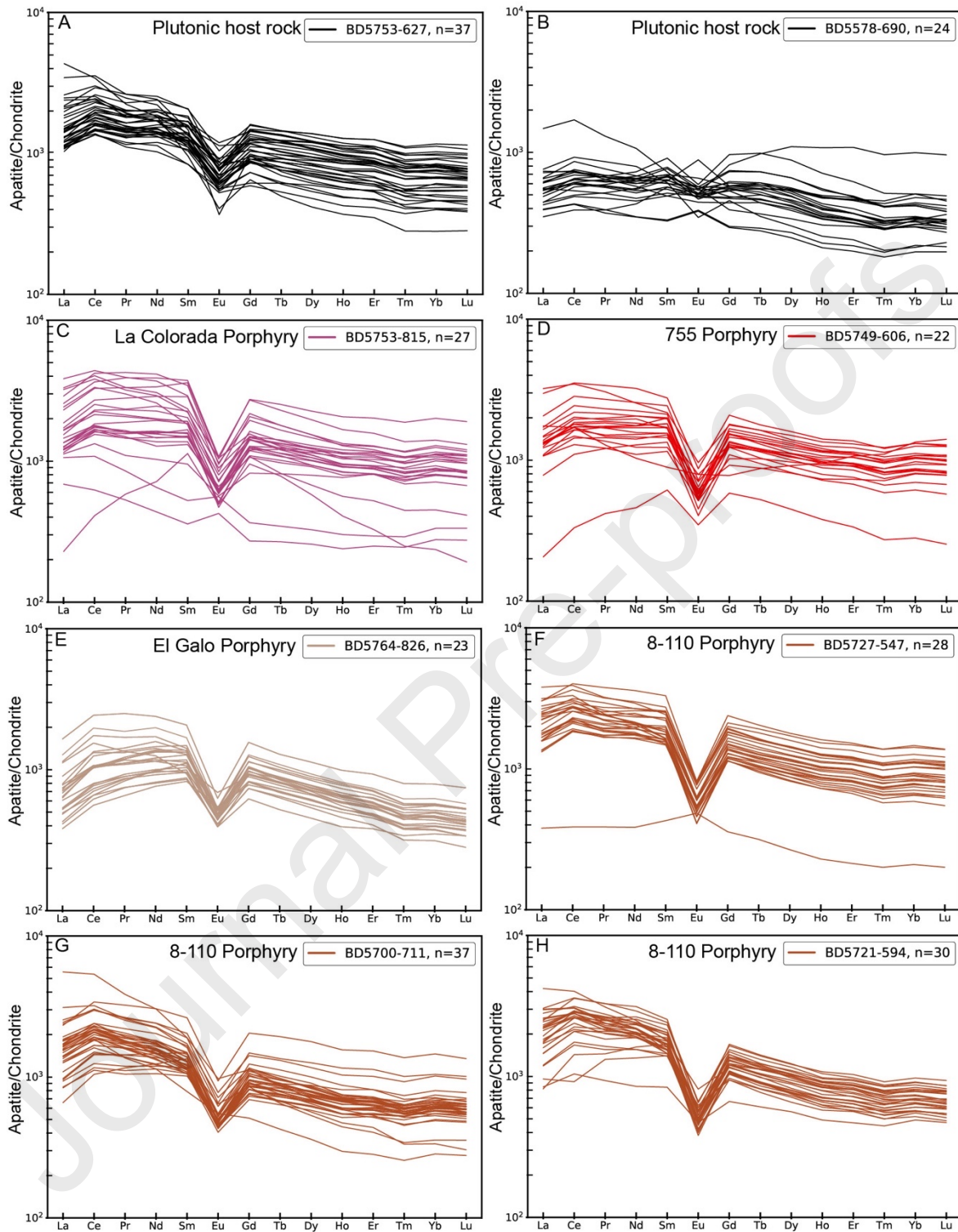
622

623 Figure 7. Tera-Wasserburg discordia plots of apatite U-Pb data results of host rocks and ore-
 624 related porphyries.

625 4.4. Apatite trace element composition

626 Apatite trace element composition data are available in Supplementary Table S6. Concerning
627 the intrusive host rocks, the REE distribution of apatite from sample BD5753-627m shows a
628 classical right-sloping REE pattern with an enrichment in LREE and a depletion in HREE
629 (Fig. 8A) with $(La/Lu)_N$ ratios ranging from 1.2 to 15.3 (median of 2.1). Eu and Ce anomalies
630 range from 0.3 to 0.8 (median 0.6) and from 1.1 to 1.3 (median 1.2), respectively. Apatite Cl
631 concentrations are lower than 1.0 wt% (median 0.5 wt%), and Sr concentrations range from
632 198 to 372 ppm (median 256 ppm). Apatite of sample BD5578-690m, another intrusive host
633 rock, shows a relatively flat REE pattern (Fig. 8B) with $(La/Lu)_N$ ratios ranging from 0.4 to
634 4.5 (median 1.7). Eu anomalies and Ce anomalies range from 0.6 to 1.5 (median 0.9) and
635 from 1.0 to 1.2 (median 1.1), respectively. Apatite Cl concentrations are below 0.7 wt%
636 (median 0.4 wt%), and Sr concentrations range from 150 to 499 ppm (median 199 ppm).

637 In the ore-rich group, apatite from La Colorada Porphyry (BD5753-815m) display a slightly
638 enriched LREE pattern compared to HREE (Fig. 8C) with $(La/Lu)_N$ ratios ranging from 1.2
639 to 5.9 (median 1.6) and $(Ce/Yb)_N$ ratios ranging from 1.6 to 7.4 (median 2.1). This sample
640 shows $(La/Sm)_N$ ratios ranging from 0.2 to 2.0 (median 0.8) and $(Dy/Yb)_N$ ratios ranging
641 from 0.9 to 2.5 (median 1.2). Eu and Ce anomalies range from 0.3 to 1.4 (median 0.4) and
642 from 1.0 to 1.3 (median 1.2), respectively. Apatite Cl concentrations are less than 0.6 wt%
643 (median 0.4 wt%; Fig. 9) and the Sr concentrations range from 273 to 531 ppm (median 352
644 ppm). The 755 Porphyry apatite grains (BD5749-606m) show a slightly enriched LREE
645 pattern compared to HREE (Fig. 8D) with $(La/Lu)_N$ ratios ranging from 0.8 to 2.5 (median
646 1.5) and $(Ce/Yb)_N$ ratios ranging from 1.2 to 2.9 (median 1.9). The $(La/Sm)_N$ ratios are
647 ranging from 0.3 to 2.0 (median 0.8) and $(Dy/Yb)_N$ ratios are ranging from 0.7 to 1.6 (median
648 1.2). Eu and Ce anomalies range from 0.3 to 1.0 (median 0.4) and from 1.1 to 1.2 (median
649 1.2), respectively. Apatite Cl concentrations are less than 0.6 wt% (median 0.4 wt%; Fig. 9)
650 and Sr concentrations range from 183 to 489 ppm (median 332 ppm). Apatites from El Galo
651 Porphyry (BD5764-826m) display a convex REE pattern with a slightly enrichment in LREE
652 compared to HREE (Fig. 8E) with $(La/Lu)_N$ ratios ranging from 1.9 to 3.3 (median 1.5) and
653 $(Ce/Yb)_N$ ratios ranging from 1.4 to 4.4 (median 2.0). This sample shows $(La/Sm)_N$ ratios
654 ranging from 0.4 to 1.2 (median 0.6) and $(Dy/Yb)_N$ ratios ranging from 1.3 to 1.8 (median
655 1.5). Eu and Ce anomalies range from 0.3 to 0.7 (median 0.4) and from 1.1 to 1.3 (median
656 1.2), respectively. Apatite Cl concentrations range from 0.1 to 0.6 wt% (median 0.4 wt%;
657 Fig. 9) and the Sr concentrations range from 195 to 263 ppm (median 218 ppm).



658

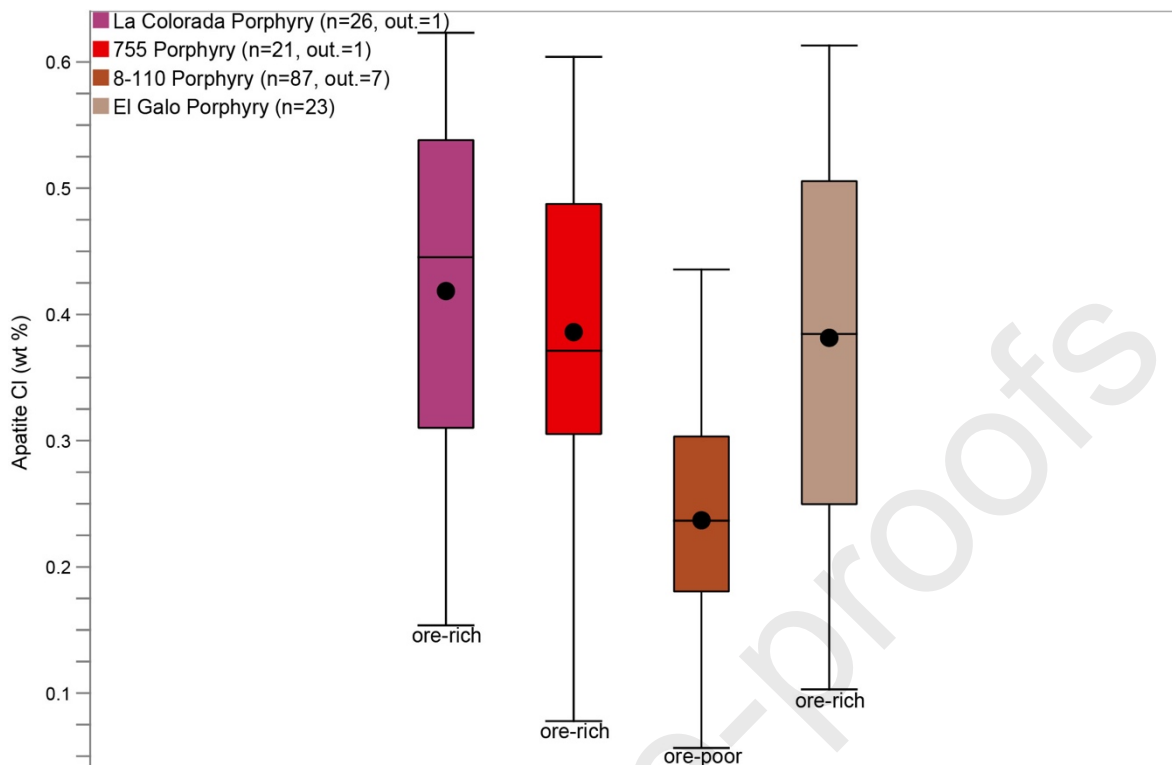
659 Figure 8. Chondrite-normalized apatite REE patterns of the intrusive host rocks and main
 660 porphyries of Buenavista del Cobre deposit. A) Sample BD5753-627m displays a classical
 661 right-sloping REE pattern. B) Sample BD5578-690m from a Jurassic pluton has a flat apatite
 662 REE pattern. Diagrams C, D, and E represent the apatite REE distributions from the ore-rich
 663 group (La Colorada, 755 and El Galo porphyries, respectively), displaying relatively flat to

664 upward convex apatite LREE distributions. Diagrams F, G, and H are apatite REE patterns
665 from the ore-poor group (8-110 Porphyry) and show right-sloping REE patterns with an
666 enrichment in LREE compared to HREE. Chondrite values are from Barrat et al. (2012).

667

668 In the ore-poor group, represented by the 8-110 Porphyry samples, apatite grains from sample
669 BD5727-547m display a right inclined REE pattern (Fig. 8F) with $(La/Lu)_N$ ratios ranging
670 from 1.3 to 4.3 (median 2.3) and $(Ce/Yb)_N$ ratios ranging from 1.8 to 4.5 (median 2.7). This
671 sample shows $(La/Sm)_N$ ratios ranging from 0.7 to 1.9 (median 1.0) and $(Dy/Yb)_N$ ratios
672 ranging from 1.2 to 1.4 (median 1.3). Eu and Ce anomalies range from 0.3 to 0.4 (median
673 0.4) and from 1.0 to 1.3 (median 1.2), respectively. Apatite Cl concentrations are less than
674 0.5 wt% (median 0.3 wt%; Fig. 9), and Sr concentrations range from 310 to 356 ppm (median
675 332 ppm). In the case of sample BD5700-711m, apatite grains show a right inclined REE
676 pattern slightly enriched in LREE compared to HREE (Fig. 8G) with $(La/Lu)_N$ ratios ranging
677 from 1.2 to 11.4 (median 2.6) and $(Ce/Yb)_N$ ratios ranging from 1.7 to 10.7 (median 3.2). The
678 $(La/Sm)_N$ ratios are ranging from 0.5 to 2.9 (median 1.2) and $(Dy/Yb)_N$ ratios are ranging
679 from 1.0 to 1.7 (median 1.2). Eu and Ce anomalies range from 0.4 to 0.9 (median 0.4) and
680 from 1.1 to 1.3 (median 1.2), respectively. The apatite Cl concentrations are less than 0.4
681 wt% (median 0.2 wt%; Fig. 9), and the Sr concentrations range from 297 to 396 ppm (median
682 327 ppm). Apatite grains from sample BD5721-574m display a right inclined apatite REE
683 pattern (Fig. 8H) with $(La/Lu)_N$ ratios ranging from 1.3 to 6.1 (median 3.1) and $(Ce/Yb)_N$
684 ratios ranging from 1.2 to 5.8 (median 3.7). The $(La/Sm)_N$ ratios are ranging from 0.5 to 2.4
685 (median 1.1) and $(Dy/Yb)_N$ ratios are ranging from 1.1 to 1.5 (median 1.3). Eu and Ce
686 anomalies range from 0.3 to 0.6 (median 0.3) and from 0.8 to 1.3 (median 1.2), respectively.
687 The apatite Cl concentrations are less than 0.4 wt% (median 0.2 wt%; Fig. 9) and the Sr
688 concentrations range from 303 to 361 ppm (median 328 ppm).

689



690
 691 Figure 9. Box plots showing the apatite chlorine composition for ore-rich and ore-poor
 692 porphyry intrusions. The central box is the middle 50% of data from the first (bottom of the
 693 box) and third (top of the box) quartiles. The black circle and line are the mean and median
 694 of the data, respectively. The whiskers are the extreme values that are not outliers. Outliers
 695 values (out.) were discarded for this comparison. Porphyries are organized from older (left)
 696 to younger (right).

697

698 5. Discussion

699 5.1. Host rocks geochronology

700 New zircon U-Pb dates obtained from the intrusive host rock of the mineralization help to
 701 support and discuss the geological observations made by several authors over the years.
 702 Sample BD5753-468m was collected from a deep exploration drill hole (Fig. 2) in the present
 703 mine operation and corresponds to a coarse-grained granitic rock that is unconformably
 704 overlain by the Henrietta Formation. This sample yielded an upper intercept age of $1422 \pm$
 705 $14/18$ Ma (Fig. 5A). The upper intercept date is equivalent to the upper intercept age of 1440
 706 ± 15 Ma reported by Anderson and Silver (1977) for the Cananea Granite in the Capote Basin.
 707 We therefore interpret it as the emplacement age of the Cananea Granite, confirming the
 708 Precambrian age of this intrusive. In the case of the lower intercept age ($111 \pm 9/9$ Ma; Fig.
 709 5A), no tectono-magmatic event that could explain lead loss has been recognized yet in the
 710 Cananea Mining District at the end of the Lower Cretaceous. For this reason, we believe that
 711 the lower intercept age recorded by the Cananea Granite possibly has no geological meaning.

712 To date, the only known outcrop of the Cananea Granite in the Cananea Mining District
713 occurs in the Capote Basin (Valentine, 1936), where it is unconformably overlain by the
714 Paleozoic strata and bordered by the NW-SE oriented Elisa and Capote Pass faults. In the
715 Capote Basin, Zn-Cu skarns mineralization developed in the Paleozoic rocks associated with
716 the emplacement of the Late Cretaceous-Paleogene magmatic-hydrothermal systems
717 (Meinert, 1980, Farfán-Panamá, 2002; Ortiz-Olvera, 2022). Recently, the Capote Pass fault
718 has been interpreted as an Oligo-Miocene south-dipping normal fault (Ortiz-Olvera, 2022).
719 If this fault displaced the Cananea Granite to the south, as suggested by its recognition in
720 drill hole exploration, then the Paleozoic sequence and its associated skarn mineralization
721 might be present below the Mesa and Henrietta Formations, east of the current open pit
722 operation (Fig. 2). This new finding highlights the importance of dating newly discovered
723 intrusive bodies as it could have important consequences, in this case increasing the
724 possibility of finding previously undiscovered Zn-Cu skarns deposits.

725 The presence of Triassic-Jurassic igneous rocks in the region of Cananea Mining District has
726 been proposed by several authors (e.g., Valentine, 1936; Meinert, 1980; Wodzicki, 1995).
727 These rocks include the volcanic rocks of the Elenita and Henrietta Formations and the El
728 Torre Syenite pluton. This assumption was made on the basis of cross-cutting relationships
729 between different rock units and their lithological similarities to rocks of Triassic-Jurassic
730 age in southern Arizona. For example, the Elenita Formation was correlated with the Late-
731 Triassic to Mid-Jurassic Mt. Wrightson Formation, which crops out in Santa Rita Mountains,
732 Arizona (Drewes, 1971). Despite the contact between Elenita Formation and Henrietta
733 formation being a fault, clasts of the Elenita Formation were reported by Valentine (1936) in
734 the lowermost Henrietta Formation, which was therefore considered to be younger. Previous
735 attempts of $^{40}\text{Ar}/^{39}\text{Ar}$ hornblende dating of the Henrietta Formation yielded ages of $57.9 \pm$
736 0.2 Ma and ~ 94 Ma, which were interpreted as a thermally reset age and a minimum
737 formation age for this unit (Wodzicki, 1995). In this study, we report for the first time a zircon
738 U-Pb age of $186.8 \pm 1.1/3.0$ Ma (Fig. 5C) that was obtained for a volcanic flow from the
739 Henrietta Formation (Fig. 2), confirming an Early Jurassic age for these rocks.

740 In addition, a Jurassic age has been proposed for the El Torre Syenite pluton based on its
741 lithologic and geochemical similarities to the granitic to syenitic plutons emplaced from 170
742 to 150 Ma in Sonora (Gastil et al., 1978; Anderson and Silver, 1978; Meinert, 1980;
743 Wodzicki, 1995). An $^{40}\text{Ar}/^{39}\text{Ar}$ hornblende age of 58.4 ± 0.5 Ma for this rock was interpreted
744 as reset age due to its similarity with the age of porphyry copper mineralization of the district,
745 whereas a ~ 70 Ma date was interpreted as a minimum formation age with a poorly defined
746 plateau (Wodzicki, 1995). In this study, samples BD5752-669m and BD5578-690m from
747 two plutonic rocks intersected at depth by two exploration drill holes (Fig. 2), yielded zircon
748 U-Pb ages of $186.9 \pm 1.3/3.1$ Ma (Fig. 5B, Table 1) and $176.3 \pm 1.1/2.9$ Ma (Fig. 5D, Table
749 1), respectively. Specifically, sample BD5578-690m corresponds to a medium to fine-
750 grained plutonic rock and is composed dominantly by K-feldspar + plagioclase + hornblende
751 \pm quartz \pm biotite and accessory zircon and apatite (Fig. 3E). This composition is similar to
752 the mineralogical composition described for the El Torre Syenite (Valentine, 1936; Meinert,
753 1982) and we thus argue for an Early Jurassic age for this intrusion. In addition, the new
754 apatite U-Pb ages obtained in this study from intrusive host rocks are 56.7 ± 4.6 Ma (sample
755 BD5753-627m, Fig. 7A, Table 1) and 54.0 ± 10.0 Ma (sample BD5578-690m, Fig. 7B, Table
756 1), and are in accordance with the previously published $^{40}\text{Ar}/^{39}\text{Ar}$ age. We therefore interpret

757 these ages as thermally reset ages due the effects of the porphyry emplacement. For this
758 reason, we prefer not to discuss apatite geochemistry of host rocks in this study because of
759 the possible compositional re-equilibration of apatites during high-temperature hydrothermal
760 alteration.

761 The Jurassic zircon U-Pb ages we obtained for both volcanic and plutonic rocks in the
762 Buenavista del Cobre deposit evidence the presence of an Early Jurassic magmatic arc at
763 Cananea latitude (Anderson and Silver, 1978; Tosdal et al., 1989; Valencia-Moreno et al.,
764 2024). It has to be noted that Jurassic porphyry copper mineralization associated with a
765 Jurassic arc magmatism has been reported ~65 km northeast of the Buenavista del Cobre
766 deposit in Bisbee, Arizona, and throughout southwestern North America (Barton et al., 2011).
767 The recognition of an Early Jurassic volcano-plutonic system in the Buenavista del Cobre
768 deposit opens the possibility of the development of a contemporaneous magmatic-
769 hydrothermal system. However, further evidence is needed to confirm the existence of such
770 an event.

771 Several authors have suggested that the Tinaja Diorite and the Cuitaca Granodiorite are part
772 of the same batholithic body and that they are the precursor magmas of the porphyry copper
773 mineralization at Cananea Mining District (Valentine, 1936; Meinert, 1982; Bushnell, 1988;
774 Wodzicki, 1995; Santillana-Villa et al., 2021). Limited geochronological data preclude
775 establishing a temporal relationship between these intrusions. The Cuitaca Granodiorite has
776 a zircon U-Pb age of ~64 Ma (Anderson and Silver, 1977; Del Rio-Salas et al., 2017). Our
777 new zircon U-Pb age of $73.8 \pm 0.6/1.3$ Ma (sample BC-22-11, Fig. 6A, Table 1) for the Tinaja
778 Diorite reveals that this intrusion was emplaced ~10 Ma earlier than the Cuitaca Granodiorite.
779 Thus, we interpret the previously reported $^{40}\text{Ar}/^{39}\text{Ar}$ hornblende age of 63.0 ± 0.4 Ma for the
780 Tinaja Diorite (Wodzicki, 1995) as a thermally reset age due to the intrusion of the Cuitaca
781 Granodiorite at ~64 Ma. In addition, a similar age of ~74 Ma (Del Río-Salas et al., 2017) was
782 obtained for the precursor pluton at the El Pilar deposit, ~40 km northwest of the Buenavista
783 del Cobre deposit (Fig. 1). Together, these data suggest that the Tinaja Diorite and El Pilar
784 intrusive rocks probably represent the onset of the magmatism related to the precursor
785 magmas of the main porphyry systems at the Cananea Mining District at ~74 Ma.

786

787 **5.2. Multiple magmatic events**

788 Giant porphyry copper deposits around the world, such as Chuquicamata (Reynolds et al.,
789 1998; Ballard et al., 2001), El Salvador (Gustafson and Hunt, 1975; Lee et al., 2017), El
790 Teniente (Maksaev et al., 2004), and Bajo de la Alumbrera (Harris et al., 2004 and 2008) are
791 the product of multiple superimposed magmatic events as indicated by zircon U-Pb dating of
792 ore-related porphyry intrusions. However, it is known that differences in emplacement ages
793 between the different porphyries that make up a porphyry copper deposit can be difficult to
794 determine, even with high-resolution methods such as zircon U-Pb SHRIMP analyses (e.g.,
795 Lee et al., 2017). Therefore, further geological evidences such as cross-cutting relationships
796 between porphyry intrusions with different mineralogy, texture and/or geochemistry, as well
797 as dating of minerals associated with alteration and mineralization are needed to reconstruct
798 the emplacement timing of the different intrusions.

799 Zircon grains from the Buenavista del Cobre porphyry rocks exhibit needle-like shapes with
800 a concentric oscillatory growth zoning (S3 Fig. 2), typical of magmatic zircon that
801 crystallized in rapidly cooling intrusions (Corfu, 2003; Nathwani et al., 2023). In addition,
802 most zircons have similar ages in the inner and outer parts of the grains, suggesting no effects
803 of zircon recrystallization on inherited grains. For these reasons, we interpret the zircon U-
804 Pb dates of the main cluster of concordant analyses as the emplacement ages of the different
805 porphyry intrusions. These new zircon U-Pb ages of porphyry rocks obtained in this study
806 do not allow us to clearly differentiate in time discrete magmatic pulses for the Buenavista
807 del Cobre deposit, as all ages overlap within the analytical error at 2σ level (Fig. 10).
808 However, as mentioned before, several porphyry phases have been recognized in the
809 Buenavista del Cobre deposit, which are distinguished by their cross-cutting relationships,
810 mineralogical compositions, textures, and their ore-poor/ore-rich natures (Valentine, 1936;
811 Ochoa-Landín and Echávarri-Pérez, 1978; Ochoa-Landín and Navarro-Meyer, 1979).
812 Considering all the disponible data, the proposed sequence of porphyry intrusions is as
813 follows: Feldspar Porphyry, La Colorada, 755, 8-110, and El Galo porphyries, and finally the
814 Coarse-grained Porphyry phase. Hereunder, we review the different arguments used to
815 establish this chronology.

816 The Feldspar Porphyry yields a zircon U-Pb age of $59.7 \pm 0.5/1.1$ Ma, which is
817 indistinguishable from the La Colorada Porphyry that yields a zircon U-Pb age of $58.9 \pm$
818 $0.5/1.0$ Ma (Fig. 10). A second group of dates from the Feldspar Porphyry, corresponding to
819 four concordant analyses, yield a concordia date of $65.1 \pm 1.0/1.5$ Ma ($n=4$, $MSWD=0.4$;
820 Fig. 6B). This date is fairly similar to the emplacement age of ~ 64 Ma of the Cuitaca
821 Granodiorite (a precursor magma of the porphyry magmas) elsewhere in the Cananea Mining
822 District (Anderson and Silver, 1977; Del Rio Salas et al., 2013). We thus suggest that this
823 older group corresponds to zircon grains that formed at depth in the Cuitaca magmatic
824 chamber and were dragged-up to shallower crustal levels during the emplacement of the
825 Feldspar Porphyry. Moreover, both zircon U-Pb ages of the Feldspar and La Colorada
826 porphyries correlate with the molybdenite Re-Os ages of 59.2 ± 0.3 Ma for a chalcopyrite +
827 pyrite + molybdenite (massive) mineral association at the top of the La Colorada breccia
828 pipe, and of 59.3 ± 0.3 Ma for a disseminated style mineralization (Barra et al., 2005; Fig.
829 10). In the case of the disseminated style Re-Os mineralization age, it is possible that the
830 emplacement of the Feldspar Porphyry marks the onset of mineralization at the Buenavista
831 del Cobre deposit at 59.3 ± 0.3 Ma. Yet, further work on the mineralization associated with
832 the Feldspar Porphyry emplacement is required to confirm or infer this possibility. Indeed,
833 since the Feldspar Porphyry is considered an ore-poor porphyry and is not spatially related
834 to the La Colorada breccia pipe, it cannot be associated with the main Cu-Mo mineralization
835 event associated with the formation of this breccia (Ochoa-Landín and Navarro-Meyer, 1979;
836 Fig. 10). In contrast, the La Colorada Porphyry is classified as an ore-rich intrusion (Fig. 10),
837 which occurs in a close spatial relationship to the La Colorada breccia pipe (Perry, 1935).
838 Additionally, the early potassic alteration in the La Colorada breccia pipe (Bushnell, 1988)
839 was dated by K/Ar on phlogopite at 59.9 ± 2.1 Ma and 58.5 ± 2.1 Ma (Damon and Mauger,
840 1966; Varela, 1972). These ages correlate well with the lower intercept apatite U-Pb age of
841 59.2 ± 2.2 Ma (sample BD5753-815m, Fig. 7C, Table 1) obtained for the La Colorada
842 Porphyry and suggest that the main Cu-Mo mineralization event at Buenavista del Cobre
843 began with the emplacement of the La Colorada Porphyry at $58.9 \pm 0.5/1.0$ Ma (zircon U-Pb
844 emplacement age of sample BD5753-815m, Fig. 6C and 10, Table 1), after the emplacement

845 of the ore-poor Feldspar Porphyry at $59.7 \pm 0.5/1.1$ Ma (zircon U-Pb emplacement age for
846 sample BD5570-613m, Fig. 6B and 10, Table 1).

847 In the case of the 755 Porphyry, we obtained a zircon U-Pb age of $57.5 \pm 0.2/0.9$ Ma (Fig.
848 6D) and an apatite U-Pb age of 58.3 ± 3.1 Ma (Fig. 7D). The zircon U-Pb age overlaps with
849 the La Colorada Porphyry emplacement age but postdates the Feldspar Porphyry
850 emplacement age (Fig. 10). This observation is in good agreement with the fact that the 755
851 Porphyry crosscuts the Feldspar Porphyry and that it shares apatite geochemical
852 characteristics with the ore-rich La Colorada Porphyry (cf. next section). One possible
853 interpretation is that the La Colorada and the 755 porphyries belong to a single porphyry
854 complex originating the main Cu mineralization event. Alternatively, these porphyries could
855 correspond to two different intrusions that were emplaced in a relatively short period of time
856 (as described for the L and K porphyries in the El Salvador deposit; Gustafson and Hunt,
857 1975; Lee et al., 2017), making it impossible to differentiate their emplacement ages by our
858 dating methods. Interestingly, it has to be noted that the 755 Porphyry zircon U-Pb
859 emplacement age does not overlap with the molybdenite Re-Os ages of the main Cu
860 mineralization event related to the La Colorada Porphyry emplacement (Fig. 10). We thus
861 consider that the emplacement of the 755 Porphyry corresponds to a different magmatic pulse
862 that might have developed a magmatic-hydrothermal system associated with a second Cu-
863 Mo mineralization event. However, further works on Re-Os and $^{40}\text{Ar}/^{39}\text{Ar}$ geochronology on
864 ore-related minerals are needed to confirm this interpretation.

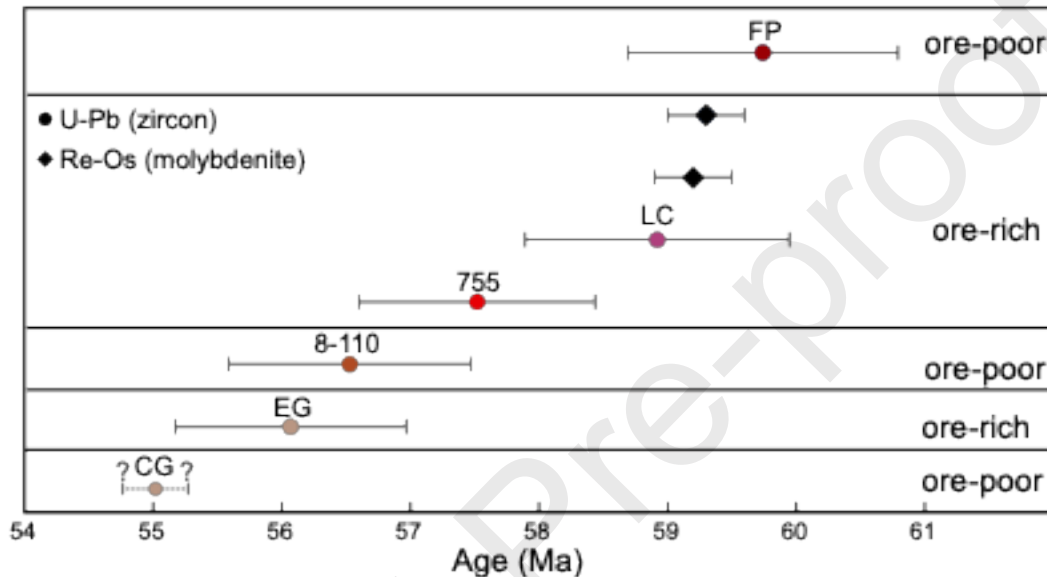
865 The 8-110 Porphyry yields a zircon U-Pb age of $56.5 \pm 0.3/0.9$ Ma (sample BD5721-574m,
866 Fig. 6E, Table 1) and three apatite U-Pb ages of 56.8 ± 2.6 Ma (sample BD5727-547m, Fig.
867 7E, Table 1), 56.8 ± 1.9 Ma (sample BD5700-711m, Fig. 7F, Table 1), and 56.0 ± 4.6 Ma
868 (sample BD5721-574m, Fig. 7G, Table 1). Additionally, the El Galo Porphyry yields a zircon
869 U-Pb age of $56.1 \pm 0.2/0.9$ Ma (sample BD5764-826m, Fig. 6F, Table 1) and an apatite U-
870 Pb age of 57.0 ± 8.2 Ma (Fig. 7H, Table 1). Considering the propagated error uncertainties,
871 these intrusions (8-110 and El Galo porphyries) are thus temporally indistinguishable from
872 the 755 Porphyry (Fig. 10), impeding defining different discrete igneous events of
873 emplacement.

874 However, the 8-110 Porphyry has historically been classified as an ore-poor porphyry
875 (Ochoa-Landín and Navarro-Meyer, 1979; Fig. 10) and exhibits apatite geochemistry
876 differences from the 755 and El Galo ore-rich porphyries (cf. next section). We also show
877 that the El Galo Porphyry emplacement is spatially associated with an ore-rich potassic
878 alteration zone (Fig. 4F), and that it shares apatite geochemical characteristics with the ore-
879 rich porphyries (La Colorada and 755 porphyries; cf. next section). Taken together, these
880 observations suggests that the emplacement of the El Galo Porphyry is related to a different
881 magmatic-hydrothermal system than the 8-110 Porphyry.

882 Moreover, the maximum age of the Cu-Mo mineralization event associated with the El Galo
883 Porphyry potassic alteration is constrained to 56 Ma as Cu and Mo sulfides veinlets cross-
884 cut the El Galo Porphyry (Fig. 4E), which has a $56.1 \pm 0.2/0.9$ Ma crystallization age (Fig.
885 6F, Table 1). This is younger than the available molybdenite Re-Os ages associated to the
886 emplacement of the La Colorada Porphyry and breccia (see above, Fig. 10). Even if there is
887 no molybdenite Re-Os date to further constrain this young mineralizing hydrothermal

888 system, we consider that at least two discrete events of mineralization occurred at Buenavista
 889 del Cobre, associated with the emplacement of the La Colorada Porphyry for the first event
 890 and with the El Galo Porphyry for the younger event (note that it is possible that another
 891 mineralizing event occurred associated with the emplacement of the 755 Porphyry).

892 Finally, the Coarse-grained Porphyry is an ore-poor porphyry intrusion, which is likely
 893 younger than the 8-110 and El Galo porphyries as it crosscuts the 8-110 Porphyry (Ochoa-
 894 Landín and Navarro-Meyer, 1979; Fig. 10). Unfortunately, we did not find any apatite and
 895 zircon crystals in this porphyry and were unable to further characterize this intrusion.



896

897 Figure 10. Emplacement (zircon U-Pb ages) and Cu-Mo mineralization timing (Re-Os ages
 898 by Barra et al., 2005) of the six known porphyry intrusions in the Buenavista del Cobre
 899 deposit. Error bars on zircon U-Pb data correspond to propagated systematics uncertainties.
 900 Abbreviations: FP (Feldspar Porphyry), LC (La Colorada Porphyry), 755 (755 Porphyry), 8-
 901 110 (8-110 Porphyry), EG (El Galo Porphyry), CG (Coarse-grained Porphyry).

902

903 5.3. Geochemistry of apatite as a fertility indicator

904 5.3.1. Magmatic oxidation state

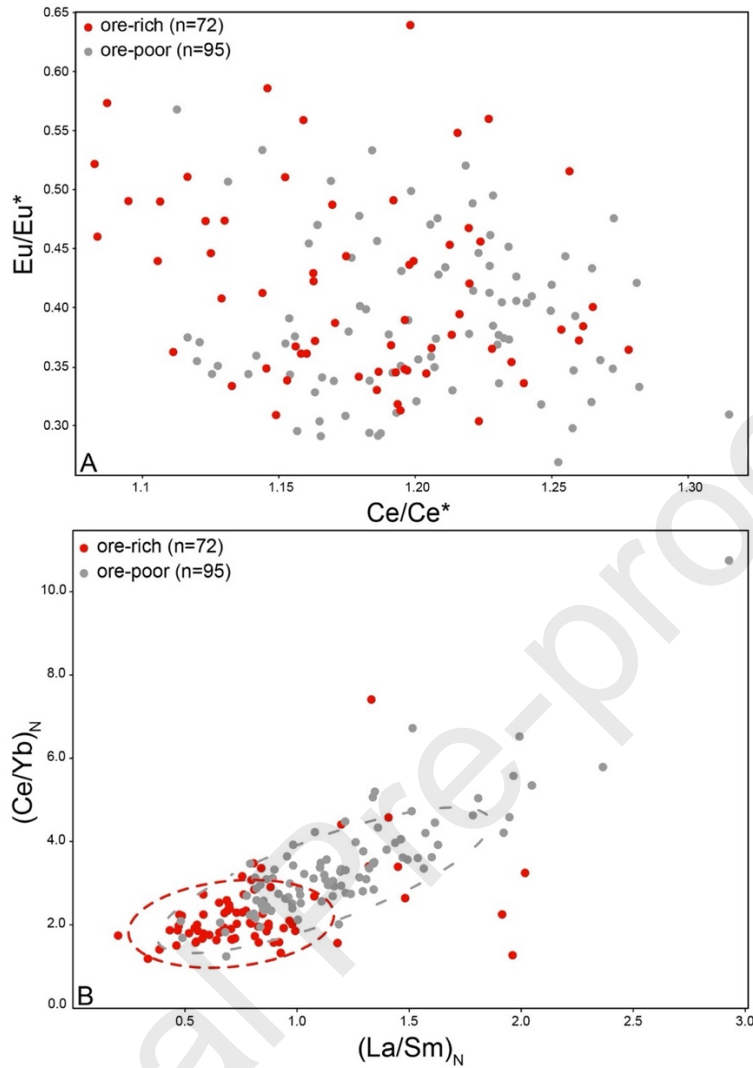
905 Apatite prefers to incorporate Eu^{3+} and Ce^{3+} rather than Eu^{2+} and Ce^{4+} because the difference
 906 in ionic radius between them and Ca^{2+} is small and they can substitute for it (Sha and Chapell,
 907 1999; Cao et al., 2012; Pan et al., 2016). Moreover, the redox ratios $\text{Eu}^{2+}/\text{Eu}^{3+}$ and $\text{Ce}^{3+}/\text{Ce}^{4+}$
 908 of a melt is a function of oxygen fugacity, temperature, pressure and composition of the melt
 909 (Sha and Chappel, 1998). Oxidized melts with high oxygen fugacity and low $\text{Eu}^{2+}/\text{Eu}^{3+}$ ratios
 910 have higher Eu^{3+} abundance than reduced melts. As apatite preferentially incorporate Eu^{3+} ,
 911 apatites crystallizing from oxidized melts are expected to present higher Eu content and thus
 912 a lower Eu anomaly than apatites crystallizing from reduced melts. The same reasoning can

913 be done for Ce in apatite: Ce^{3+}/Ce^{4+} of oxidized melts is low and their Ce^{3+} content (which
914 preferentially partitions in apatite) is low, thus apatites crystallizing from an oxidized melt
915 are expected to exhibit low Ce content and thus higher Ce anomalies than apatites from
916 reduced melts. As a result, apatite chemistry has been used as a proxy for the oxidation state
917 of magmas using Eu and Ce anomalies (e.g., Sha and Chappell, 1999; Cao et al., 2012; Pan et
918 al., 2016).

919 In Buenavista del Cobre, the Eu and Ce anomalies (Eu/Eu^* and Ce/Ce^* values) of apatite
920 from ore-rich and ore-poor intrusions overlap with no clear difference between the two
921 groups (Fig. 11A). These results suggest that the magmatic oxidation states of the porphyritic
922 magmas were similar and that Eu and Ce anomalies cannot be used in our case as good
923 fertility indicators to distinguish ore-rich from ore-poor magmas. This also suggests that
924 other factors such as the magma H_2O content are more important at the deposit scale than the
925 magma oxidation state (e.g., Richards, 2011).

926 **5.3.2. Apatite REE signature**

927 In contrast to the relative oxidation state of the magmas, an evaluation of the general apatite
928 REE composition of ore-rich and ore-poor porphyries allows us to distinguish two fields with
929 specific $(La/Sm)_N$ and $(Ce/Yb)_N$ signatures (Fig. 11B). As REE are incompatible elements,
930 and because LREE are more incompatible than HREE, these values allow to track the relative
931 differentiation of melts. Apatites from the ore-poor group show a more fractionated REE
932 distribution ($(Ce/Yb)_N=1.2-10.7$; median 3.1) with a slight LREE enrichment compared to
933 apatites from the ore-rich group ($(Ce/Yb)_N=1.2$ to 7.4; median 2.0). In addition, the ore-poor
934 apatite show a higher LREE concentrations and MREE depletion with higher $(La/Sm)_N$ ratios
935 (0.5 to 2.9; median 1.1) than apatites from ore-rich porphyries ($(La/Sm)_N=0.2$ to 2.0; median
936 0.8). These findings suggest that the ore-poor porphyries experienced a higher degree of
937 LREE fractionation and therefore, a higher degree of magmatic differentiation compared to
938 ore-rich porphyries. However, this interpretation is at odds with the fact that Cu is an
939 incompatible element and should concentrate in the melts the more differentiated from the
940 parental magma (e.g., Richards 2003). We instead propose that the apatite trace element
941 composition difference between ore-rich and ore-poor magmas is controlled by petrogenetic
942 processes such as crystal fractionation of specific REE-bearing and hydrous or anhydrous
943 mineral phases in the parental melt (eg., Sha and Chappell, 1999; Sun et al., 2022; Quan et
944 al., 2023). Indeed, mineral fractionation is known to influence the concentration of REE and
945 volatiles such as the H_2O in residual magmas which affects the transport of metals and
946 magma fertility. We explore this possible interpretation in the next section.



947

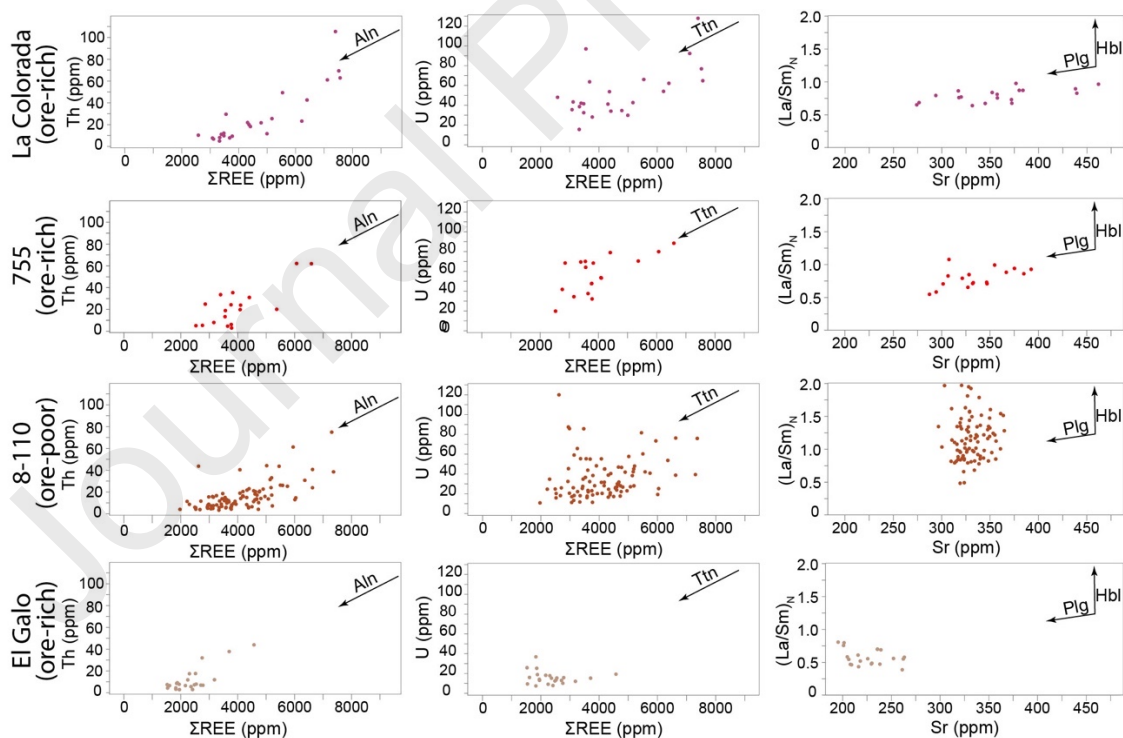
948 Figure 11. Apatite Ce vs Eu anomalies and $(La/Sm)_N$ vs $(Ce/Yb)_N$ ratios plots. Red and gray
 949 dotted lines represent the Mahalanobis contour ellipses with a p -value=0.95 showing the data
 950 outliers for the ore-rich and ore-poor groups, respectively.

951

952 5.3.3. Fractional crystallization process of porphyry magmas sources

953 Apatite trace element content (such as Sr, Th, U, and REE) can be used as a geochemical
 954 index to trace the mineral crystallization sequence involved in the petrogenesis of granitic
 955 rocks (Nathwani et al., 2020; Sun et al., 2022; Quan et al., 2023), which may control the
 956 fertility of porphyritic magmas. Indeed, trace elements composition of apatite depends on the
 957 mineral phases that crystallized before or at the same time as apatite (e.g., Pan et al., 2016;
 958 Nathwani et al., 2020; Zhang et al., 2020; Sun et al., 2022; Quan et al., 2023). In particular,
 959 accessory minerals such as monazite, allanite, titanite, and zircon can incorporate REE, U,
 960 and Th in their crystalline structure and compete with apatite during magma crystallization
 961 (Sha and Chappell, 1999; Sun et al., 2022 and references therein).

962 In Buenavista del Cobre, apatite grains from ore-rich and ore-poor groups, show positive
 963 correlation between REE and Th, and between REE and U (Fig. 12); suggesting the co-
 964 crystallization of accessory minerals that may compete with apatite incorporating these
 965 elements (Sha and Chappell, 1999; Sun et al., 2022 and references therein). The
 966 crystallization of monazite, which could play a role in Th incorporation, is unlikely because
 967 of the calc-alkaline nature of the porphyry magmas, an unusual environment for monazite
 968 crystallization (Sha and Chappell, 1998). Moreover, experimental studies suggest that zircon
 969 typically crystallizes later than apatite during the cooling of continental arc magmas (e.g.,
 970 Lee and Bachmann, 2014), limiting the influence of zircon crystallization on the U and Th
 971 composition of apatite. Allanite may also crystallize at the same time or before apatite,
 972 incorporating REE as well as Th. Actually, the normalized apatite REE patterns of all
 973 samples show a depletion in La (Fig. 8C-H) and a positive correlation between Th and total
 974 REE composition (Fig. 12), which are consistent with allanite crystallization (e.g., Cao et al.,
 975 2012; Quan et al., 2023). Finally, if titanite crystallizes before or at the same time as apatite,
 976 the composition of the latter will show a positive correlation between U and total REE
 977 composition (Quan et al., 2023; Fig. 12). Titanite crystallization is typical of oxidized
 978 magmas (Wones, 1989). Our results are thus in agreement with the relatively high oxidation
 979 state expected for the source of porphyry magmas. However, if crystal fractionation of titanite
 980 and allanite in the parental magma promotes the formation of porphyritic melts (e.g., Cao et
 981 al., 2012), it does not have any effect on the porphyry magmas fertility (both ore-poor and
 982 ore-rich porphyries show titanite and allanite fractionation signature) because it only controls
 983 the REE budget of the magma, which does not affect metal solubility.

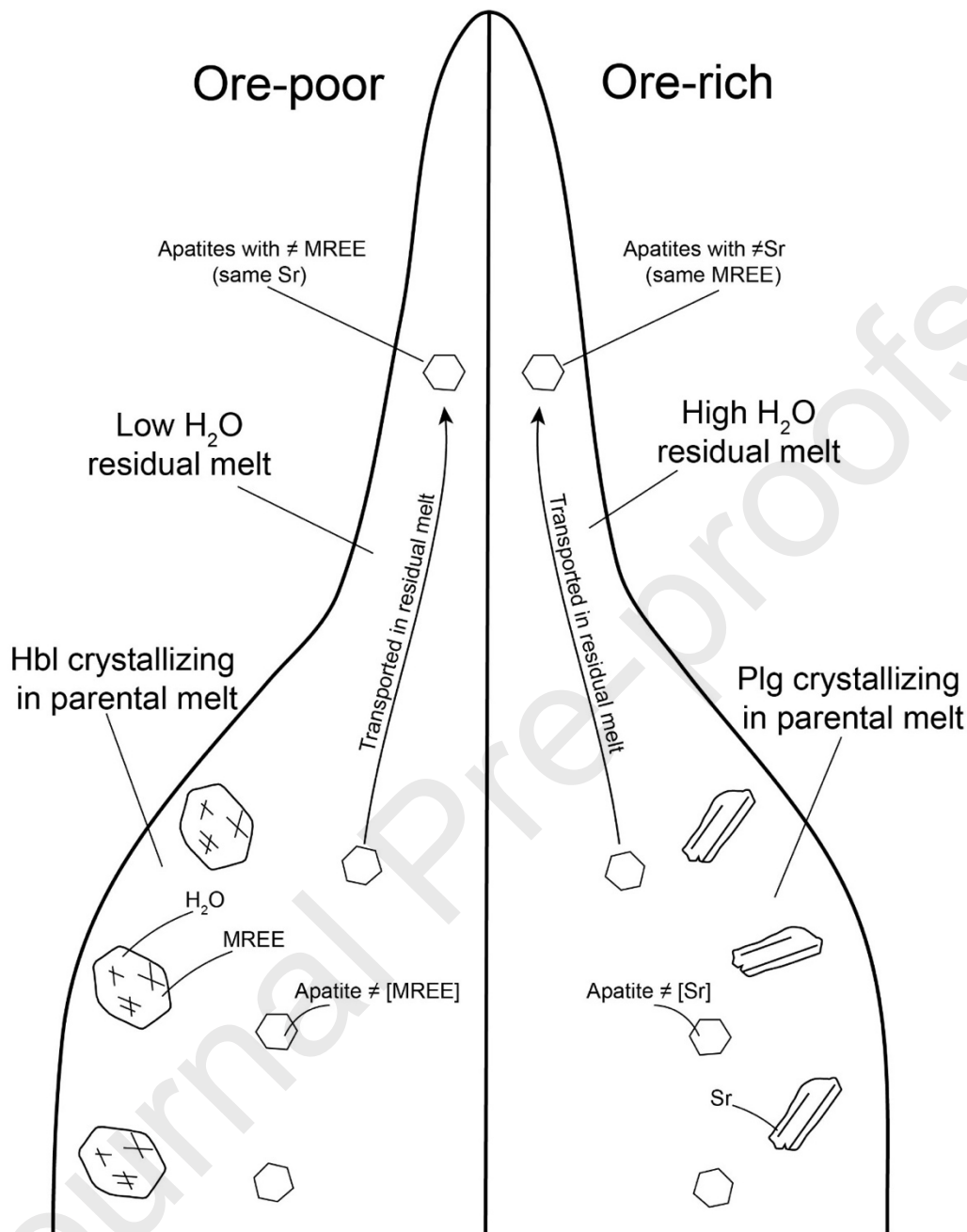


984

985 Figure 12. Different plots used to track the fractionation of different mineral phases that
 986 compete with apatite for trace element incorporation (REE composition, $(La/Sm)_N$ ratios, Sr,
 987 U and Th concentrations). Abbreviations: Aln= allanite; Ttn=titanite.

988 In porphyry copper deposits, metal solubility increases with the H₂O content of causative
989 magmas. The initial H₂O content of a melt is related to its origin at deep crustal levels (in the
990 MASH zone; Cloos, 2001; Richards, 2003 and 2011; Sillitoe, 2010). At shallower crustal
991 levels, in the parental magma chamber, crystallization of anhydrous minerals such as
992 plagioclase tends to increase the H₂O content of the residual magma, whereas crystallization
993 of hydrous minerals such as hornblende removes H₂O from the melt (Cloos, 2001; Tosdal
994 and Richards, 2001). On one hand, when apatite crystallizes from a melt dominated by
995 plagioclase fractionation, Sr and to a lesser extent LREE tend to be retained in plagioclase,
996 which induces a large spread in apatite Sr contents (Sha and Chappell, 1999; Belousova,
997 2001; Pan et al., 2016; Sun et al., 2022; Quan et al., 2023). On the other hand, hornblende
998 tends to incorporate MREE, and when apatite crystallizes from a melt dominated by
999 hornblende fractionation, apatite will exhibit a large spread in the (La/Sm)_N ratios as
1000 consequence of MREE depletion (Sun et al., 2022).

1001 In the Buenavista del Cobre porphyritic bodies, apatite commonly occurs as sub-rounded
1002 inclusions within major minerals (quartz, feldspars and hornblendes; S1 Fig. 3) suggesting
1003 that apatite crystallized at depth and were transported by the porphyritic melt. If this
1004 interpretation is correct, the apatite chemistry must reflect the petrogenetic processes that
1005 occurred at depth, and at the origin of the different metal budgets of the porphyritic magmas.
1006 The ore-poor 8-110 Porphyry yielded apatite showing a hornblende fractionation signature
1007 (Fig. 12), whereas all the apatites from ore-rich porphyry intrusions show Sr contents and
1008 REE patterns indicating plagioclase fractionation (Fig. 12). This can be explained by the fact
1009 that crystallization of hydrated mineral phases such as hornblendes at depth results in a low-
1010 fluid content residual melt, lowering the potential of magmatic-hydrothermal activity and
1011 inhibiting metal mobilization, fluid exsolution and mineralization at shallow crustal levels
1012 (Fig. 13). In contrast, crystallization at depth of anhydrous mineral phases such as plagioclase
1013 increases the fluid content of the residual melt, which in turn increases metal mobilization
1014 and promotes high-grade mineralization in hydrothermal systems at shallower crustal levels
1015 (Fig. 13). Thus, we interpret that in the Buenavista del Cobre deposit the ore-poor and ore-
1016 rich porphyry magmas are the product of parental magmas in which hornblende and
1017 plagioclase crystallized, respectively.



1018

1019 Figure 13. Timing of apatite crystallization relative to hornblende and plagioclase
 1020 fractionation in the parental magma of ore-poor vs ore-rich porphyries. Apatite co-
 1021 crystallizing with hornblende exhibit a wide range in MREE concentrations (≠[MREE]), the
 1022 residual magma present low H₂O content, impeding metal transportation and promoting the
 1023 formation of an ore-poor porphyry. When plagioclase, which preferentially incorporates Sr,
 1024 crystallizes at the same time as apatite, the latter show a wide range in their Sr content (≠[Sr]).
 1025 As plagioclase is an anhydrous mineral, its crystallization leads to a H₂O content increase
 1026 and favors Cu solubility in the residual melt leading to the formation of ore-rich porphyry
 1027 magmas. Note that in this model, apatite crystals crystallized at depth and are transported to

1028 shallower crustal levels at the time of the porphyry emplacement (as indicated by the
1029 occurrence of apatite as sub-rounded inclusions in the major minerals of the porphyry rocks).

1030 **5.3.4. Apatite Cl content**

1031 The Cl content of the porphyry magmas is often used to assess their fertility because Cl forms
1032 complexes with metals such as Cu and determines the metal transport capacity of magmas
1033 and hydrothermal fluids (e.g., Shinohara, 1994; Williams et al., 1995; Chelle-Michou and
1034 Chiaradia, 2017). Apatite can record the volatile content of magmas due to its ability to
1035 incorporate elements such as Cl, S and F (e.g., Sha and Chappel, 1999). Figure 9 shows the
1036 variation in apatite chlorine content of the different porphyry intrusions at the Buenavista del
1037 Cobre deposit. During the first fertile stage of Cu-Mo mineralization, the La Colorada and
1038 the 755 ore-rich porphyries have slightly high apatite Cl (median=0.4 wt%) concentrations
1039 (Fig. 9). Subsequently, the ore-poor 8-110 Porphyry emplacement is associated with a
1040 slightly lower apatite Cl concentrations (median= 0.2 wt%). The apatite Cl concentration
1041 increases again (median= 0.4 wt%) with the emplacement of the El Galo ore-rich Porphyry.
1042 These results show that apatite from the ore-rich porphyries have slightly higher magmatic
1043 Cl-contents than those from the ore-poor porphyries. This observation highlights the
1044 importance of magmatic chlorine content as an important factor in the magma fertility and in
1045 the development of an ore-rich porphyry intrusion.

1046 **5.4 Genetic model of the Buenavista del Cobre deposit**

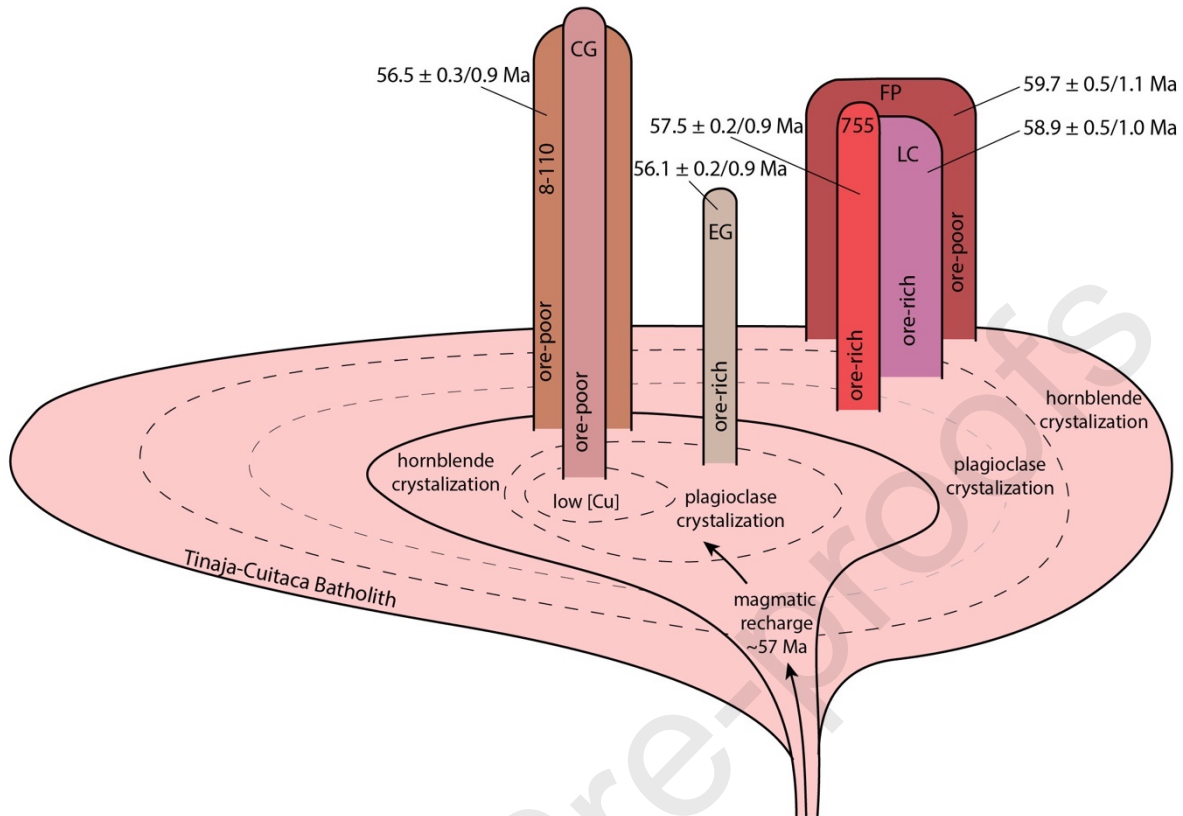
1047 Based on cross-cutting relationships, zircon U-Pb geochronology and apatite geochemistry,
1048 we propose that the mineralization of Buenavista del Cobre deposit is the result of the
1049 emplacement of several porphyry intrusions within a period of at least 4 Ma (Fig. 14). Apatite
1050 geochemistry indicate that ore-poor and ore-rich porphyry intrusions record a different
1051 magmatic evolution. Indeed, all porphyry intrusions share similar magmatic oxidation states
1052 (as shown by the overlapping of apatite Eu and Ce anomalies; Fig. 11A) but exhibit
1053 differences in emplacement time, and apatite Sr and REE signatures (Fig. 11B and 12). We
1054 propose that these characteristics reflects changing petrogenetic processes through time.

1055 The porphyry intrusions sequence probably began with the emplacement of the ore-poor
1056 Feldspar Porphyry at $59.7 \pm 0.5/1.1$ Ma (Fig. 14). Despite the lack of apatite in this porphyry
1057 because of acid alteration, we speculate that the injection of a hot, hydrous (>5.5 wt% H₂O)
1058 mafic magma into the upper crust during the early stages of the magmatic system may have
1059 promoted the crystallization of high temperature hydrated minerals as hornblendes in the
1060 absence of plagioclase fractionation, which crystallizes at lower temperatures (e.g., Loucks,
1061 2014; Fig. 14). As previously discussed, this process can remove some of the H₂O volume
1062 (retained in the crystals) of the residual magma, resulting in a subsequent ore-poor porphyry
1063 intrusion. In porphyry copper systems, it is common for the early porphyry intrusions to be
1064 poorly mineralized and for the well-mineralized porphyries to develop at later stages of the
1065 magmatic evolution (e.g., El Salvador; Gustafson and Hunt, 1975; Lee et al., 2017).

1066 At Buenavista del Cobre, we suspect that as the temperature of the parental magma (Tinaja-
1067 Cuitaca Batholith) decreases with inward crystallization and magma differentiation in a
1068 closed system, there was a change in magma composition towards a more evolved

1069 composition, leading to plagioclase fractionation (Fig. 14). As plagioclase is an anhydrous
1070 mineral, this process allowed fluid exsolution and accumulation in the residual magma. At
1071 high temperature and pressure Cu is soluble in the fluid phase (Williams et al., 1995), as a
1072 result, porphyry copper melts issued from plagioclase-dominated fractional crystallization
1073 tend to produce ore-rich porphyry intrusions. Cross-cutting relationships indicate that a
1074 period of Cu-Mo fertility began after the emplacement of the Feldspar Porphyry, associated
1075 with the emplacement of the ore-rich La Colorada Porphyry at $58.9 \pm 0.5/1.0$ Ma (Fig. 14).
1076 In addition, the ore-rich 755 Porphyry probably represent another magmatic pulse with an
1077 emplacement age of $57.5 \pm 0.2/0.9$ Ma as this crystallization age does not overlap with the
1078 mineralization age of the La Colorada breccia pipe (Fig. 10). Apatite geochemistry in both
1079 intrusions indicates plagioclase fractionation, which explains their ore-rich character (Fig.
1080 14). Moreover, anhydrous mineral fractionation can promote H₂O but also a volatile content
1081 increase in the residual magma. This is evidenced by the high apatite Cl content of the La
1082 Colorada and 755 porphyry intrusions (Fig. 9). As these ore-rich porphyries are not separated
1083 by a known ore-poor porphyry, we consider that their emplacement time correspond to a long
1084 period of Cu-Mo productivity at the Buenavista del Cobre deposit (Fig. 14). Interestingly, at
1085 the Mariquita porphyry copper deposit (Fig. 1) which has estimated resources of about 58 Mt
1086 of Cu at 0.4-0.6% (Aponte-Barrera, 2009), the age of mineralization has been constrained by
1087 two Re-Os molybdenite ages between 59.2 ± 0.3 Ma and 59.3 ± 0.3 Ma (Del Rio-Salas et al.,
1088 2017). These mineralization ages are in good agreement with the timing of the mineralization
1089 (~59 Ma) associated with the La Colorada porphyry emplacement and suggest a productive
1090 period of Cu-Mo mineralization at the batholithic scale.

1091 At $56.5 \pm 0.3/0.9$ Ma, the ore-poor 8-110 Porphyry was emplaced. This intrusion is
1092 characterized by an apatite geochemical signature indicating hornblende fractionation at
1093 depth (Fig. 12). Moreover, the low Cl content of apatite in this intrusion (Fig. 9) is in good
1094 agreement with its ore-poor character as a low-Cl magma composition implies a limited metal
1095 transport capacity in the exsolved fluids as there are less chlorine complexes available
1096 (Shinohara, 1994; Williams et al., 1995). We thus propose that the 8-110 intrusion followed
1097 a magmatic recharge of the batholith (and probably magma mixing?) at ~57 Ma, and the
1098 beginning of a new magmatic cycle (Fig. 14). This recharge triggered the resumption of
1099 hornblende crystallization at depth. After a period of fractional crystallization from which
1100 the 8-110 ore-poor Porphyry was produced, a new period of Cu-Mo productivity began when
1101 the evolving batholithic magma composition allowed plagioclase fractionation. Increased
1102 H₂O exsolution triggered the emplacement of the ore-rich El Galo Porphyry at $56.1 \pm 0.2/0.9$
1103 Ma (Fig. 14), characterized by apatite with relatively high Cl content (Fig. 9). We propose
1104 that the end of the magmatic-hydrothermal system is marked by the emplacement of the ore-
1105 poor Coarse-grained Porphyry (Fig. 14). We interpret the absence of Cu mineralization
1106 associated with the emplacement of this intrusion as reflecting the fluids and metals
1107 exhaustion at the end of the magmatic cycle (Fig. 14).



1108

1109 Figure 14. Petrogenetic model for the formation of the Buenavista del Cobre porphyry copper
 1110 deposit. A first magmatic cycle involving hornblende partial crystallization followed by
 1111 plagioclase partial crystallization produced a sequence of ore-poor and ore-rich porphyry
 1112 intrusions represented by the Feldspar Porphyry (FP), and La Colorada (LC) and 755
 1113 porphyries, respectively. A magmatic recharge of the batholith at ca. 57 Ma triggered a new
 1114 sequence of ore-poor followed by ore-rich porphyries intrusions corresponding to the 8-110
 1115 Porphyry and El Galo Porphyry (EG), respectively. The end of the magmatic-hydrothermal
 1116 system is marked by the emplacement of the ore-poor Coarse-grained Porphyry (CG), the
 1117 scarce sulfide mineralization in this intrusion reflecting the fluids and metals exhaustion at
 1118 the end of the magmatic cycle.

1119

1120 6. Conclusions

1121 The Buenavista del Cobre porphyry Cu-Mo deposit is the result of the superposition of
 1122 multiple magmatic-hydrothermal pulses over a period of at least 4 Ma. The proposed genetic
 1123 model involves two cycles of supply, cooling and partial crystallization of the parental
 1124 magma of the porphyry intrusions and gives new insights on the petrogenetic processes at
 1125 the origin of porphyry magma fertility. Fractional crystallization process of the parental
 1126 magma influences the fertility of the porphyry magmas, resulting in the formation of ore-rich
 1127 or ore-poor porphyry intrusions. The evolution of the parental melt by fractional
 1128 crystallization of plagioclase increases the H₂O content of the residual magma resulting in

1129 the formation of ore-rich porphyritic intrusions. In contrast, hornblende fractionation leads
1130 to the formation of ore-poor porphyritic intrusions.

1131 The variations of apatite REE signatures (such as $(Ce/Yb)_N$ and $(La/Sm)_N$ ratios) and trace
1132 element composition (such as Sr and Cl, U and Th) can be used to track petrogenetic
1133 processes involved in the formation of an economic porphyry copper deposit. This
1134 contribution further supports that petrogenetic processes controlling porphyry copper
1135 magmas fertility are recorded in the composition of apatite at a deposit scale and highlights
1136 the importance of considering apatite geochemistry as an exploration tool.

1137 In addition, the recognition of the Cananea granite below the present-day pit at Buenavista
1138 del Cobre deposit indicates that the skarn Zn-Cu mineralization hosted in the Paleozoic
1139 sequence might be present below the Mesa and Henrietta Formations in the eastern part of
1140 the deposit. Finally, the confirmation of the presence of the Cordilleran Jurassic magmatic
1141 arc at Cananea latitudes increases the possibility of finding undiscovered Jurassic magmatic-
1142 hydrothermal systems in the Cananea Mining District.

1143

1144 **Declaration of competing interest**

1145 VAG was hosted free of charge during two months at the Buenavista del Cobre facilities.
1146 EBM is employed by Grupo Mexico, the operating company where he is serving as
1147 *Superintendente de Geología*. MN, TC, NC, and MP declare they have no conflict of interests
1148 that are relevant to the content of this manuscript.

1149

1150 **Acknowledgments**

1151 VAG thanks CONAHCYT for a PhD grant (No. CVU: 852920). This study was partly funded
1152 by Grupo México through the PERUMEX project agreement between Grupo México and the
1153 Universidad Nacional Autónoma de México (UNAM). Travelling grants between Mexico
1154 and France were awarded by CONAHCYT, the ANUIES and the Comité ECOS-Nord
1155 through the project ECOS-Nord 322545 / M22U01. MN thanks the DGAPA-UNAM for
1156 funding the project PAPIIT IA105324 that partly funded field expenses. The authors
1157 especially thank Mario Rascón-Heimpel, Alfonso Martínez-Vera, and Cristo Bejarano-
1158 Carrillo for their help in securing funding. Sample preparation was supported by the
1159 LANGEM and we warmly thank E. González-Becuar and A. Orcí-Romero for their technical
1160 help. The authors thank Gaby Gutiérrez, Mario Quijada, Andrea Esparza, Mario Garcia,
1161 Alejandro Torres and Adolfo Gastélum of the geological department of the Buenavista del
1162 Cobre mine for provided guidance and valuable help during field work. The authors also wish
1163 to thank the Editor-in-Chief Dr. Huayong Chen, associate editor Dr. Bo Xu, Dr. Max
1164 Verdugo and two anonymous reviewers for providing valuable reviews that greatly improved
1165 the manuscript.

1166

1167 **References**

- 1168 Anderson, T. H., and Silver, L. T. (1981). An overview of Precambrian rocks in
1169 Sonora. *Revista Mexicana de Ciencias Geológicas*, 5(2), 131-139.
- 1170 Anderson, T. H., and Silver, L. T. (1977). U-Pb isotope ages of granitic plutons near Cananea,
1171 Sonora. *Economic Geology*, 72(5), 827-836. <https://doi.org/10.2113/gsecongeo.72.5.827>
- 1172 Anderson, T.H., Rodríguez-Castañeda, J.L. and Silver, L.T. (2005). Jurassic rocks in Sonora,
1173 Mexico—relations to the Mojave- Sonora megashear and its inferred northwestward
1174 extension, in Anderson, T.H.; McKee, J.W.; y Steiner, M.B., eds., The Mojave-Sonora
1175 megashear hypothesis: development, assessment, and alternatives: *Geological Society of*
1176 *America Special Paper* 393, 51–95. <https://doi.org/10.1130/0-8137-2393-0.51> }
- 1177 Aponte-Barrera, M., 2009. Geología y mineralización del yacimiento Mariquita, distrito de
1178 Cananea: In Clark, K.F., Salas-Pizá, G.A., Cubillas-Estrada, R. (eds.): *Geología Económica*
1179 *de México: Servicio Geológico Mexicano*, p. 852–856
- 1180
- 1181 Ayala-Fontes, 2009. Geología y mineralización en el distrito minero Cananea, Sonora,
1182 México. In: Clark, K.F., Salas-Pizá, G.A., Cubillas-Estrada, R. (Eds.), *Geología Económica*
1183 *de México. Servicio Geológico Mexicano*, pp. 804–810.
- 1184
- 1185 Ballard, J. R., Palin, J. M., Williams, I. S., Campbell, I. H., and Faunes, A. (2001). Two ages
1186 of porphyry intrusion resolved for the super-giant Chuquicamata copper deposit of northern
1187 Chile by ELA-ICP-MS and SHRIMP. *Geology*, 29(5), 383-386.
1188 [https://doi.org/10.1130/0091-7613\(2001\)029<0383:TAOPIR>2.0.CO;2](https://doi.org/10.1130/0091-7613(2001)029<0383:TAOPIR>2.0.CO;2)
- 1189
- 1190 Barra, F., Ruiz, J., Valencia, V. A., Ochoa-Landín, L., Chesley, J. T., and Zurcher, L. (2005).
1191 Laramide porphyry Cu-Mo mineralization in northern Mexico: Age constraints from Re-Os
1192 geochronology in molybdenite. *Economic Geology*, 100(8), 1605-1616.
1193 <https://doi.org/10.2113/gsecongeo.100.8.1605>
- 1194
- 1195 Barrat, J. A., Zanda, B., Moynier, F., Bollinger, C., Liorzou, C., and Bayon, G. (2012).
1196 Geochemistry of CI chondrites: Major and trace elements, and Cu and Zn
1197 isotopes. *Geochimica et Cosmochimica Acta*, 83, 79-92.
1198 <https://doi.org/10.1016/j.gca.2011.12.011>
- 1199

- 1200 Barton, M. D., Girardi, J. D., Kreiner, D. C., Seedorff, E., Zurcher, L., Dilles, J. H., Haxel,
1201 G., and Johnson, D. (2011). Jurassic igneous-related metallogeny of southwestern North
1202 America. *Great Basin Evolution and Metallogeny: Reno, Nevada, Geological Society of*
1203 *Nevada*, 373-396.
- 1204 Belousova, E. A., Walters, S., Griffin, W. L., and O'reilly, S. Y. (2001). Trace-element
1205 signatures of apatites in granitoids from the Mt Isa Inlier, northwestern
1206 Queensland. *Australian Journal of Earth Sciences*, 48(4), 603-619.
1207 <https://doi.org/10.1046/j.1440-0952.2001.00879.x>
- 1208 Belousova, E. A., Griffin, W. L., O'Reilly, S. Y., and Fisher, N. I. (2002). Apatite as an
1209 indicator mineral for mineral exploration: trace-element compositions and their relationship
1210 to host rock type. *Journal of Geochemical Exploration*, 76(1), 45-69.
1211 [https://doi.org/10.1016/S0375-6742\(02\)00204-2](https://doi.org/10.1016/S0375-6742(02)00204-2)
- 1212 Boehnke, P., and Harrison, T. M. (2014). A meta-analysis of geochronologically relevant
1213 half-lives: what's the best decay constant?. *International Geology Review*, 56(7), 905-914.
1214 <https://doi.org/10.1080/00206814.2014.908420>
- 1215 Bouzari, F., Hart, C. J., Bissig, T., and Barker, S. (2017). Hydrothermal alteration revealed
1216 by apatite luminescence and chemistry: A potential indicator mineral for exploring covered
1217 porphyry copper deposits. *Economic Geology*, 111(6), 1397-1410.
1218 <https://doi.org/10.2113/econgeo.111.6.1397>
- 1219
- 1220 Brass, G. W., Mattes, B. W., Reid, R. P., and Whitman, J. M. (1983). Mesozoic interaction
1221 of the Kula Plate and the western margin of North America. *Tectonophysics*, 99(2-4), 231-
1222 239. [https://doi.org/10.1016/0040-1951\(83\)90105-1](https://doi.org/10.1016/0040-1951(83)90105-1)
- 1223
- 1224 Bruand, E., Fowler, M., Storey, C., and Darling, J. (2017). Apatite trace element and isotope
1225 applications to petrogenesis and provenance. *American Mineralogist*, 102(1), 75-84.
1226 <https://doi.org/10.2138/am-2017-5744>
- 1227
- 1228 Bushnell, S. E. (1988). Mineralization at Cananea, Sonora, and the paragenesis and zoning
1229 of breccia pipes in quartzofeldspathic rock. *Economic Geology*, 83(8), 1760-1781.
1230 <https://doi.org/10.2113/gsecongeo.83.8.1760>
- 1231
- 1232 Cao, M., Li, G., Qin, K., Seitmuratova, E. Y., and Liu, Y. (2012). Major and trace element
1233 characteristics of apatites in granitoids from Central Kazakhstan: implications for
1234 petrogenesis and mineralization. *Resource Geology*, 62(1), 63-83.
1235 <https://doi.org/10.1111/j.1751-3928.2011.00180.x>

1236

1237 Carreón-Pallares, J. N. (2002). *Structure and tectonic history of the Milpillas porphyry*
1238 *copper district, Sonora, Mexico: Salt Lake City, University of Utah* (Doctoral dissertation,
1239 MS thesis, 72 p).

1240

1241• Chelle-Michou, C., and Chiaradia, M. (2017). Amphibole and apatite insights into the
1242 evolution and mass balance of Cl and S in magmas associated with porphyry copper
1243 deposits. *Contributions to Mineralogy and Petrology*, 172(11), 105.
1244 <https://doi.org/10.1007/s00410-017-1417-2>

1245

1246 Chew, D. M., Petrus, J. A., and Kamber, B. S. (2014). U–Pb LA–ICPMS dating using
1247 accessory mineral standards with variable common Pb. *Chemical Geology*, 363, 185-199.
1248 <https://doi.org/10.1016/j.chemgeo.2013.11.006>

1249

1250 Chew, D. M., Donelick, R. A., Donelick, M. B., Kamber, B. S., and Stock, M. J. (2014).
1251 Apatite chlorine concentration measurements by LA-ICP-MS. *Geostandards and*
1252 *Geoanalytical Research*, 38(1), 23-35. <https://doi.org/10.1111/j.1751-908X.2013.00246.x>

1253 Cloos, M. (2001). Bubbling magma chambers, cupolas, and porphyry copper
1254 deposits. *International geology review*, 43(4), 285-311.
1255 <https://doi.org/10.1080/00206810109465015>

1256 Cogné, N., Chew, D. M., Donelick, R. A., and Ansberque, C. (2020). LA-ICP-MS apatite
1257 fission track dating: A practical zeta-based approach. *Chemical Geology*, 531, 119302.
1258 <https://doi.org/10.1016/j.chemgeo.2019.119302>

1259

1260 Cogné, N., Derycke, A., and Gallagher, K. (2024). The McClure Mountain Syenite Apatite
1261 as a Potential Age Control Reference Material for LA-ICP-MS AFT and U-Pb Double
1262 Dating. *Geostandards and Geoanalytical Research*. <https://doi.org/10.1111/ggr.12545>

1263

1264 Coney, P. J., and Reynolds, S. J. (1977). Cordilleran benioff zones. *Nature*, 270(5636), 403-
1265 406. <https://doi.org/10.1038/270403a0>

1266

- 1267 Coney, P. J., and Harms, T. A. (1984). Cordilleran metamorphic core complexes: Cenozoic
1268 extensional relics of Mesozoic compression. *Geology*, 12(9), 550-554.
1269 [https://doi.org/10.1130/0091-7613\(1984\)12<550:CMCCCE>2.0.CO;2](https://doi.org/10.1130/0091-7613(1984)12<550:CMCCCE>2.0.CO;2)
- 1270
- 1271 Correa-García, J. P. (1983). Distribución del molibdeno en el distrito minero de Cananea,
1272 Sonora. Universidad de Sonora, Tesis de licenciatura (65 pp.).
- 1273
- 1274 Corfu, F., Hanchar, J. M., Hoskin, P. W., and Kinny, P. (2003). Atlas of zircon
1275 textures. *Reviews in mineralogy and geochemistry*, 53(1), 469-500.
1276 <https://doi.org/10.2113/0530469>
- 1277
- 1278 Cox, D. P., Miller, R. J., and Woodbourne, K. L. (2006). *The Laramide Mesa Formation and*
1279 *the Ojo de Agua Caldera, Southeast of the Cananea Copper Mining District, Sonora, Mexico.*
1280 US Geological Survey. <https://doi.org/10.3133/sir20065022>
- 1281
- 1282 Damon, P. E., and Mauger, R. L. (1966). Epeirogeny-orogeny viewed from the Basin and
1283 Range province. *Trans Am Inst Min metall Engrs*, 235, 99-112.
- 1284
- 1285 Del Rio-Salas, R., Ochoa-Landín, L., Ruiz, J., Eastoe, C., Meza-Figueroa, D., Zuñiga-
1286 Hernández, H., Mendivil-Quijada, H., and Quintanar-Ruiz, F. (2013). Geology, stable
1287 isotope, and U–Pb geochronology of the Mariquita porphyry copper and Lucy Cu–Mo
1288 deposits, Cananea District, Mexico: a contribution to regional exploration. *Journal of*
1289 *Geochemical Exploration*, 124, 140-154. <https://doi.org/10.1016/j.gexplo.2012.08.016>
- 1290
- 1291 Del Rio-Salas, R., Ochoa-Landín, L., Valencia-Moreno, M., Calmus, T., Meza-Figueroa, D.,
1292 Salgado-Souto, S., Kirk, J., Ruiz, J., and Mendivil-Quijada, H. (2017). New U–Pb and Re–
1293 Os geochronology of Laramide porphyry copper mineralization along the Cananea
1294 lineament, northeastern Sonora, Mexico: Contribution to the understanding of the Cananea
1295 copper district. *Ore Geology Reviews*, 81, 1125-1136.
1296 <https://doi.org/10.1016/j.oregeorev.2015.11.029>
- 1297
- 1298 Drewes, H. (1971). *Mesozoic stratigraphy of the Santa Rita Mountains, southeast of Tucson,*
1299 *Arizona.* In: U.S. Geological Survey Professional Paper, 658-C, 81 pp.
- 1300

- 1301 Eisele, J., and Isachsen, C.E., (2001). Crustal growth in southern Arizona: U-Pb
1302 geochronologic and Sm-Nd isotopic evidence for addition of the Paleoproterozoic Cochise
1303 block to the Mazatzal Province, *American Journal of Earth Sciences*, 310, 773–797.
1304 [10.2475/AJS.301.9.773](https://doi.org/10.2475/AJS.301.9.773)
- 1305
- 1306 Emmons, S. F. (1910). Cananea mining district of Sonora, Mexico. *Economic Geology*, 5(4),
1307 312-356. <https://doi.org/10.2113/gsecongeo.5.4.312>
- 1308
- 1309 Engebretson, D. C., Cox, A., and Gordon, R. G. (1985). Relative motions between oceanic
1310 and continental plates in the Pacific basin. *Geological Society of America Special Paper*, 206,
1311 1-59. <https://doi.org/10.1130/SPE206-p1>
- 1312
- 1313 Farfán-Panamá, J.L. (2002). Caracterización de los yacimientos en Skarn de Buenavista en
1314 Cananea, Son. Universidad de Sonora, tesis de maestría, 113 pp.
- 1315
- 1316 Ferrari, L., Orozco-Esquivel, T., Bryan, S. E., Lopez-Martinez, M., and Silva-Fragoso, A.
1317 (2018). Cenozoic magmatism and extension in western Mexico: Linking the Sierra Madre
1318 Occidental silicic large igneous province and the Comondú Group with the Gulf of California
1319 rift. *Earth-Science Reviews*, 183, 115-152. <https://doi.org/10.1016/j.earscirev.2017.04.006>
- 1320
- 1321 Gans, P. B. (1997). Large-magnitude Oligo-Miocene extension in southern Sonora:
1322 Implications for the tectonic evolution of northwest Mexico. *Tectonics*, 16(3), 388-408.
1323 <https://doi.org/10.1029/97TC00496>
- 1324
- 1325 Gastil, R. G., Morgan, G. J., and Krummenacher, D. (1978). Mesozoic history of peninsular
1326 California and related areas east of the Gulf of California. In *Mesozoic paleogeography of*
1327 *the western United States: Pacific Section, Society of Economic Paleontologists and*
1328 *Mineralogists, Pacific Coast Paleogeography Symposium* (Vol. 2, pp. 107-116).
- 1329 Gustafson, L. B., and Hunt, J. P. (1975). The porphyry copper deposit at El Salvador,
1330 Chile. *Economic geology*, 70(5), 857-912. <https://doi.org/10.2113/gsecongeo.70.5.857>
- 1331 Harris, A. C., Allen, C. M., Bryan, S. E., Campbell, I. H., Holcombe, R. J., and Palin, J. M.
1332 (2004). ELA-ICP-MS U–Pb zircon geochronology of regional volcanism hosting the Bajo
1333 de la Alumbreira Cu–Au deposit: implications for porphyry-related

- 1334 mineralization. *Mineralium Deposita*, 39, 46-67. [https://doi.org/10.1007/s00126-003-0381-](https://doi.org/10.1007/s00126-003-0381-0)
1335 [0](https://doi.org/10.1007/s00126-003-0381-0)
- 1336 Harris, A. C., Dunlap, W. J., Reiners, P. W., Allen, C. M., Cooke, D. R., White, N. C.,
1337 Campbell, I.H., and Golding, S. D. (2008). Multimillion year thermal history of a porphyry
1338 copper deposit: application of U–Pb, $^{40}\text{Ar}/^{39}\text{Ar}$ and (U–Th)/He chronometers, Bajo de la
1339 Alumbra copper–gold deposit, Argentina. *Mineralium Deposita*, 43, 295-314.
1340 <https://doi.org/10.1007/s00126-007-0151-5>
- 1341 Horstwood, M. S., Košler, J., Gehrels, G., Jackson, S. E., McLean, N. M., Paton, C., Pearson,
1342 N.J., Sircombe, K., Sylvester, P., Vermeesch, P., Bowring, J.F., Condon, D.J., and Schoene,
1343 B. (2016). Community-derived standards for LA-ICP-MS U-(Th) Pb geochronology–
1344 Uncertainty propagation, age interpretation and data reporting. *Geostandards and*
1345 *Geoanalytical Research*, 40(3), 311-332. <https://doi.org/10.1111/j.1751-908X.2016.00379.x>
- 1346
- 1347 Keith, S. B., and Swan, M. M. (1995). Tectonic setting, petrology, and genesis of the
1348 Laramide porphyry copper cluster of Arizona, Sonora, and New Mexico. *Porphyry copper*
1349 *deposits of the American Cordillera: Arizona Geological Society Digest*, 20, 339-346.
- 1350
- 1351 Klemme, S., John, T., Wessels, M., Kusebauch, C., Berndt, J., Rohrbach, A., and Schmid-
1352 Beurmann, P. (2013). Synthesis of trace element bearing single crystals of Chlor-Apatite (Ca
1353 $_{5}$ (PO $_{4}$) $_{3}$ Cl) using the flux growth method. *Chemistry Central Journal*, 7, 1-6.
1354 <https://doi.org/10.1186/1752-153X-7-56>
- 1355
- 1356 Jackson, S. E., Pearson, N. J., Griffin, W. L., and Belousova, E. A. (2004). The application
1357 of laser ablation-inductively coupled plasma-mass spectrometry to in situ U–Pb zircon
1358 geochronology. *Chemical geology*, 211(1-2), 47-69.
1359 <https://doi.org/10.1016/j.chemgeo.2004.06.017>
- 1360 Jochum, K. P., Weis, U., Stoll, B., Kuzmin, D., Yang, Q., Raczek, I., Jacob, D.R., Stracke,
1361 A., Birbaum, K., Frick, D.A., Günther, D.,ENZWEILER, J. (2011). Determination of reference
1362 values for NIST SRM 610–617 glasses following ISO guidelines. *Geostandards and*
1363 *Geoanalytical Research*, 35(4), 397-429. <https://doi.org/10.1111/j.1751-908X.2011.00120.x>
- 1364 Lang, J. R., and Tittley, S. R. (1998). Isotopic and geochemical characteristics of Laramide
1365 magmatic systems in Arizona and implications for the genesis of porphyry copper
1366 deposits. *Economic Geology*, 93(2), 138-170. <https://doi.org/10.2113/gsecongeo.93.2.138>
- 1367 Lee, R. G., Dilles, J. H., Tosdal, R. M., Wooden, J. L., and Mazdab, F. K. (2017). Magmatic
1368 evolution of granodiorite intrusions at the El Salvador porphyry copper deposit, Chile, based
1369 on trace element composition and U/Pb age of zircons. *Economic Geology*, 112(2), 245-273.
1370 <https://doi.org/10.2113/econgeo.112.2.245>

- 1371 Lee, C. T. A., & Bachmann, O. (2014). How important is the role of crystal fractionation in
 1372 making intermediate magmas? Insights from Zr and P systematics. *Earth and Planetary*
 1373 *Science Letters*, 393, 266-274. <https://doi.org/10.1016/j.epsl.2014.02.044>
- 1374 Leveille, R. A., and Stegen, R. J. (2012). "The Southwestern North America Porphyry
 1375 Copper Province", *Geology and Genesis of Major Copper Deposits and Districts of the*
 1376 *World: A Tribute to Richard H. Sillitoe, Jeffrey W. Hedenquist, Michael Harris, Francisco*
 1377 *Camus. Society of Economic Geologists Special Publication*, 16, pp. 361-401.
 1378 <https://doi.org/10.5382/SP.16.15>
- 1379 Loader, M. (2017). Mineral indicators of porphyry Cu fertility. (Doctoral dissertation,
 1380 Imperial College London) (436 pp.).
- 1381 Lodders, K. (2010). Solar system abundances of the elements. In *Principles and Perspectives*
 1382 *in Cosmochemistry: Lecture Notes of the Kodai School on 'Synthesis of Elements in Stars'*
 1383 *held at Kodaikanal Observatory, India, April 29-May 13, 2008* (pp. 379-417). Springer
 1384 Berlin Heidelberg. https://doi.org/10.1007/978-3-642-10352-0_8
- 1385• Loucks, R. R. (2014). Distinctive composition of copper-ore-forming arc
 1386 magmas. *Australian Journal of Earth Sciences*, 61(1), 5-16.
 1387 <https://doi.org/10.1080/08120099.2013.865676>
- 1388 Maksaev, V., Munizaga, F., McWilliams, M., Fanning, M., Mathur, R., Ruiz, J., and Zentilli,
 1389 M. (2004). New chronology for El Teniente, Chilean Andes, from U-Pb, 40Ar/39Ar, Re-Os,
 1390 and fission-track dating: Implications for the evolution of a supergiant porphyry Cu-Mo
 1391 deposit. In: Sillitoe, R. H., Perelló, J., & Vidal, C. E. (Eds.) *Andean Metallogeny: New*
 1392 *Discoveries, Concepts, and Updates, Society of Economic Geologists*, 11, pp. 15-54.
 1393 <https://doi.org/10.5382/SP.11.02>
- 1394
- 1395 Mao, M., Rukhlov, A. S., Rowins, S. M., Spence, J., and Coogan, L. A. (2016). Apatite trace
 1396 element compositions: A robust new tool for mineral exploration. *Economic*
 1397 *Geology*, 111(5), 1187-1222. <https://doi.org/10.2113/econgeo.111.5.1187>
- 1398 McDowell, F. W., Roldán-Quintana, J., and Amaya-Martínez, R. (1997). Interrelationship of
 1399 sedimentary and volcanic deposits associated with Tertiary extension in Sonora,
 1400 Mexico. *Geological Society of America Bulletin*, 109(10), 1349-1360.
 1401 [https://doi.org/10.1130/0016-7606\(1997\)109<1349:IOSAVD>2.3.CO;2](https://doi.org/10.1130/0016-7606(1997)109<1349:IOSAVD>2.3.CO;2)
- 1402 McDowell, F. W., Roldán-Quintana, J., and Connelly, J. N. (2001). Duration of Late
 1403 Cretaceous–early Tertiary magmatism in east-central Sonora, Mexico. *Geological Society of*
 1404 *America Bulletin*, 113(4), 521-531. [https://doi.org/10.1130/0016-](https://doi.org/10.1130/0016-7606(2001)113<0521:DOLCET>2.0.CO;2)
 1405 [7606\(2001\)113<0521:DOLCET>2.0.CO;2](https://doi.org/10.1130/0016-7606(2001)113<0521:DOLCET>2.0.CO;2)
- 1406

- 1407 McDowell, F. W., McIntosh, W. C., and Farley, K. A. (2005). A precise ^{40}Ar – ^{39}Ar
1408 reference age for the Durango apatite (U–Th)/He and fission-track dating standard. *Chemical*
1409 *Geology*, 214(3-4), 249-263. <https://doi.org/10.1016/j.chemgeo.2004.10.002>
- 1410
- 1411 Meinert, L. D. (1980). *Skarn, manto, and breccia pipe formation in sedimentary rocks in the*
1412 *Cananea District, Sonora, Mexico*. Unpublished PhD dissertation, Stanford University, pp.
1413 232.
- 1414
- 1415 Meinert, L. D. (1982). Skarn, manto, and breccia pipe formation in sedimentary rocks of the
1416 Cananea mining district, Sonora, Mexico. *Economic Geology*, 77(4), 919-949.
1417 <https://doi.org/10.2113/gsecongeo.77.4.919>
- 1418
- 1419 Nathwani, C. L., Loader, M. A., Wilkinson, J. J., Buret, Y., Sievwright, R. H., and Hollings,
1420 P. (2020). Multi-stage arc magma evolution recorded by apatite in volcanic
1421 rocks. *Geology*, 48(4), 323-327. <https://doi.org/10.1130/G46998.1>
- 1422
- 1423 Nathwani, C. L., Wilkinson, J. J., Brownscombe, W., and John, C. M. (2023). Mineral texture
1424 classification using deep convolutional neural networks: an application to zircons from
1425 porphyry copper deposits. *Journal of Geophysical Research: Solid Earth*, 128(2),
1426 e2022JB025933. <https://doi.org/10.1029/2022JB025933>
- 1427
- 1428 Nosenzo, F., Manzotti, P., Poujol, M., Ballèvre, M., and Langlade, J. (2022). A window into
1429 an older orogenic cycle: P–T conditions and timing of the pre-Alpine history of the Dora-
1430 Maira Massif (Western Alps). *Journal of metamorphic geology*, 40(4), 789-821.
1431 <https://doi.org/10.1111/jmg.12646>
- 1432
- 1433 Noguez-Alcántara, B. (2008). Reconstrucción del modelo genético y evolución tectónica del
1434 yacimiento tipo pórfido cuprífero Milpillas, Distrito de Cananea, Sonora, Mexico:
1435 Hermosillo, Sonora, Mexico, Posgrado en Ciencias de la Tierra, Universidad Nacional
1436 Autónoma de México. *Unpublished Ph. D. Thesis, Universidad Nacional Autónoma de*
1437 *México, (390 pp.)*.
- 1438

- 1439 Nourse, J. A., Anderson, T. H., and Silver, L. T. (1994). Tertiary metamorphic core
1440 complexes in Sonora, northwestern Mexico. *Tectonics*, 13(5), 1161-1182.
1441 <https://doi.org/10.1029/93TC03324>
- 1442
- 1443 Ochoa-Landín, L., and Echávarri, A. (1978). Observaciones preliminares sobre la secuencia
1444 de las intrusiones hipabisales en el Tajo Colorada-veta del distrito minero de Cananea:
1445 Hermosillo, México, Universidad de Sonora. *Boletín del Departamento de Geología*, 1, 57-
1446 60.
- 1447
- 1448 Ochoa-Landín, L., and Navarro-Mayer, A. (1979). Historia geológica y tectónica del distrito
1449 de Cananea y alteración y mineralización de los tajos Colorada-Veta y Kino: Universidad de
1450 Sonora. *Boletín del Departamento de Geología*, 2(2), 150-184.
- 1451
- 1452 Ortiz-Olvera, V. (2022). Estudio petrográfico, geoquímico y estructural del depósito de tipo
1453 skarn de Buenavista zinc, Cananea, Sonora. Universidad Nacional Autónoma de México.
1454 Tesis de maestría, (161 pp).
- 1455
- 1456 Pan, L. C., Hu, R. Z., Wang, X. S., Bi, X. W., Zhu, J. J., and Li, C. (2016). Apatite trace
1457 element and halogen compositions as petrogenetic-metallogenic indicators: Examples from
1458 four granite plutons in the Sanjiang region, SW China. *Lithos*, 254, 118-130.
1459 <https://doi.org/10.1016/j.lithos.2016.03.010>
- 1460
- 1461 Paton, C., Hellstrom, J., Paul, B., Woodhead, J., and Hergt, J. (2011). Iolite: Freeware for the
1462 visualisation and processing of mass spectrometric data. *Journal of Analytical Atomic*
1463 *Spectrometry*, 26(12), 2508-2518. <https://doi.org/10.1039/C1JA10172B>
- 1464
- 1465 Perry, V. D. (1935). Copper deposits of the Cananea district Sonora, Mex. In *Sixteenth Inter-*
1466 *national Geol. Congress, Copper Resources of World* (Vol. 1, pp. 413-418).
- 1467
- 1468 Perry, V.D., 1961. The significance of mineralized breccia pipes: *Mining Eng.*, 13:367–376.
- 1469
- 1470 Piccoli, P. M., and Candela, P. A. (2002). Apatite in igneous systems. *Reviews in Mineralogy*
1471 *and Geochemistry*, 48(1), 255-292. <https://doi.org/10.2138/rmg.2002.48.6>

1472

1473 Proffett, J. M. (2003). Geology of the Bajo de la Alumbreira porphyry copper-gold deposit,
1474 Argentina. *Economic Geology*, 98(8), 1535-1574.
1475 <https://doi.org/10.2113/gsecongeo.98.8.1535>

1476

1477 Prowatke, S., and Klemme, S. (2006). Trace element partitioning between apatite and silicate
1478 melts. *Geochimica et Cosmochimica Acta*, 70(17), 4513-4527.
1479 <https://doi.org/10.1016/j.gca.2006.06.162>

1480

1481 Quan, Y., Yang, D., Yan, X., Wang, A., Hao, L., Yang, H., Wang, F., and Xu, W. (2023).
1482 Petrogenesis of Mesozoic granitoids in the northeastern North China Craton: Constraints
1483 from apatite trace elements and in-situ Nd isotopic data. *Lithos*, 450, 107190.
1484 <https://doi.org/10.1016/j.lithos.2023.107190>

1485 Reynolds, P., Ravenhurst, C., Zentilli, M., and Lindsay, D. (1998). High-precision
1486 $^{40}\text{Ar}/^{39}\text{Ar}$ dating of two consecutive hydrothermal events in the Chuquicamata porphyry
1487 copper system, Chile. *Chemical Geology*, 148(1-2), 45-60. [https://doi.org/10.1016/S0009-
1488 2541\(97\)00129-0](https://doi.org/10.1016/S0009-2541(97)00129-0)

1489

1490 Richards, J. P. (2003). Tectono-magmatic precursors for porphyry Cu-(Mo-Au) deposit
1491 formation. *Economic geology*, 98(8), 1515-1533.
1492 <https://doi.org/10.2113/gsecongeo.98.8.1515>

1493

1494 Richards, J. P. (2011). High Sr/Y arc magmas and porphyry Cu±Mo±Au deposits: Just add
1495 water. *Economic Geology*, 106(7), 1075-1081. <https://doi.org/10.2113/econgeo.106.7.1075>

1496

1497 Rodríguez-Castañeda, J.L., and Anderson, T.H. (2011). El arco magmático jurásico en
1498 Sonora, México — Distribución, edades y ambiente tectónico, in Calmus, Thierry, ed.,
1499 Panorama de la geología de Sonora, México: Universidad Nacional Autónoma de México,
1500 *Instituto de Geología, Boletín 118*(4), 81–111.

1501 Santillana-Villa, C., Valencia-Moreno, M., Del Rio-Salas, R., and Ochoa-Landín, L. (2021).
1502 Geochemical variations of precursor and ore-related intrusive rocks associated with porphyry
1503 copper deposits in Sonora, northwestern Mexico. *Journal of South American Earth
1504 Sciences*, 105, 102823. <https://doi.org/10.1016/j.jsames.2020.102823>

1505

- 1506 Schwartz, G. M. (1947). Hydrothermal alteration in the " porphyry copper"
1507 deposits. *Economic Geology*, 42(4), 319-352. <https://doi.org/10.2113/gsecongeo.42.4.319>
- 1508
- 1509 Sha, L. K., and Chappell, B. W. (1999). Apatite chemical composition, determined by
1510 electron microprobe and laser-ablation inductively coupled plasma mass spectrometry, as a
1511 probe into granite petrogenesis. *Geochimica et Cosmochimica Acta*, 63(22), 3861-3881.
1512 [https://doi.org/10.1016/S0016-7037\(99\)00210-0](https://doi.org/10.1016/S0016-7037(99)00210-0)
- 1513
- 1514 Schoene, B., and Bowring, S. A. (2006). U–Pb systematics of the McClure Mountain syenite:
1515 thermochronological constraints on the age of the 40 Ar/39 Ar standard
1516 MMhb. *Contributions to Mineralogy and Petrology*, 151, 615-630.
1517 <https://doi.org/10.1007/s00410-006-0077-4>
- 1518
- 1519 Shinohara, H. (1994). Exsolution of immiscible vapor and liquid phases from a crystallizing
1520 silicate melt: Implications for chlorine and metal transport. *Geochimica et Cosmochimica*
1521 *Acta*, 58(23), 5215-5221. [https://doi.org/10.1016/0016-7037\(94\)90306-9](https://doi.org/10.1016/0016-7037(94)90306-9)
- 1522
- 1523 Sillitoe, R. H. (2010). Porphyry copper systems. *Economic geology*, 105(1), 3-41.
1524 <https://doi.org/10.2113/gsecongeo.105.1.3>
- 1525 Silver, L. T., and Chappell, B. W. (1988). The Peninsular Ranges Batholith: an insight into
1526 the evolution of the Cordilleran batholiths of southwestern North America. *Earth and*
1527 *Environmental Science Transactions of the Royal Society of Edinburgh*, 79(2-3), 105-121.
1528 <https://doi.org/10.1017/S0263593300014152>
- 1529
- 1530 Singer, D. A., Berger, V. I., and Moring, B. C. (2005). Porphyry copper deposits of the world:
1531 database, map, and grade and tonnage models. *US Geological Survey open-file report*,
1532 2005, 1060(9).
- 1533
- 1534 Sláma, J., Košler, J., Condon, D. J., Crowley, J. L., Gerdes, A., Hanchar, J. M., Horstwood,
1535 S.A., Morris, G.A., Nasdala, L., Norberg, N., Schaltegger, U., Schoene, B., Tubrett, M.N.,
1536 and Whitehouse, M. J. (2008). Plešovice zircon—a new natural reference material for U–Pb
1537 and Hf isotopic microanalysis. *Chemical Geology*, 249(1-2), 1-35.
1538 <https://doi.org/10.1016/j.chemgeo.2007.11.005>
- 1539

- 1540 Stewart, J. H. (1988). Latest Proterozoic and Paleozoic southern margin of North America
1541 and the accretion of Mexico. *Geology*, 16(2), 186-189. [https://doi.org/10.1130/0091-](https://doi.org/10.1130/0091-7613(1988)016<0186:LPAPSM>2.3.CO;2)
1542 [7613\(1988\)016<0186:LPAPSM>2.3.CO;2](https://doi.org/10.1130/0091-7613(1988)016<0186:LPAPSM>2.3.CO;2)
- 1543
- 1544 Stock, J., and Molnar, P. (1988). Uncertainties and implications of the Late Cretaceous and
1545 Tertiary position of North America relative to the Farallon, Kula, and Pacific
1546 plates. *Tectonics*, 7(6), 1339-1384. <https://doi.org/10.1029/TC007i006p01339>
- 1547
- 1548 Sonder, L. J., and Jones, C. H. (1999). Western United States extension: How the west was
1549 widened. *Annual Review of Earth and Planetary Sciences*, 27(1), 417-462.
1550 <https://doi.org/10.1146/annurev.earth.27.1.417>
- 1551
- 1552 Sun, C. Y., Cawood, P. A., Xu, W. L., Zhang, X. M., Tang, J., Li, Y., Sun, Z., and Xu, T.
1553 (2022). In situ geochemical composition of apatite in granitoids from the eastern Central
1554 Asian Orogenic Belt: A window into petrogenesis. *Geochimica et Cosmochimica Acta*, 317,
1555 552-573. <https://doi.org/10.1016/j.gca.2021.10.028>
- 1556
- 1557 Thomson, S. N., Gehrels, G. E., Ruiz, J., and Buchwaldt, R. (2012). Routine low-damage
1558 apatite U-Pb dating using laser ablation–multicollector–ICPMS. *Geochemistry, Geophysics,*
1559 *Geosystems*, 13, 1-23. <https://doi.org/10.1029/2011GC003928>
- 1560
- 1561 Tosdal, R. M., Haxel, G. B., Wright, J. E., Jenney, J. P., and Reynolds, S. J. (1989). Jurassic
1562 geology of the Sonoran Desert region, southern Arizona, southeastern California, and
1563 northernmost Sonora: Construction of a continental-margin magmatic arc. *Geologic*
1564 *evolution of Arizona: Arizona Geological Society Digest*, 17, 397-434.
- 1565
- 1566 Tosdal, R. M., and Richards, J. P. (2001). Magmatic and structural controls on the
1567 development of porphyry Cu ± Mo ± Au deposits. In: Richards, J.P., Tosdal, R.M. (Eds.),
1568 Structural Controls on Ore Genesis: Society of Economic Geologists. Reviews in Economic
1569 Geology vol. 14, pp. 157-181. <https://doi.org/10.5382/Rev.14.06>
- 1570
- 1571 Valencia-Moreno, M., López-Martínez, M., Orozco-Esquivel, T., Ferrari, L., Calmus, T.,
1572 Noury, M., and Mendivil-Quijada, H. (2021). The Cretaceous-Eocene Mexican Magmatic

- 1573 Arc: Conceptual framework from geochemical and geochronological data of plutonic
1574 rocks. *Earth-Science Reviews*, 103721. <https://doi.org/10.1016/j.earscirev.2021.103721>
- 1575
- 1576 Valencia, V. A., Noguez-Alcántara, B., Barra, F., Ruiz, J., Gehrels, G., Quintanar, F., and
1577 Valencia-Moreno, M. (2006). Re-Os molybdenite and LA-ICPMS-MC U-Pb zircon
1578 geochronology for the Milpillas porphyry copper deposit: insights for the timing of
1579 mineralization in the Cananea District, Sonora, Mexico. *Revista mexicana de ciencias*
1580 *geológicas*, 23(1), 39-53.
- 1581
- 1582 Valencia-Moreno, M., Camprubí, A., Ochoa-Landín, L., Calmus, T., and Mendivil-Quijada,
1583 H. (2016). Latest Cretaceous-early Paleogene “boom” of porphyry Cu mineralization
1584 associated with the Laramide magmatic arc of Mexico. *Ore Geology Reviews*, 81, 1113-
1585 1124. <https://doi.org/10.1016/j.oregeorev.2016.05.005>
- 1586 Valencia-Moreno, M., González-León, C. M., Solari, L., Rascón-Heimpel, M. A., González-
1587 Becuar, E., Lozano-Santacruz, R., & Pérez-Arvizu, O. (2024). U–Pb zircon geochronology
1588 and geochemistry of the Jurassic magmatic rocks from the region of Cananea and Nacozari,
1589 northeastern Sonora, Mexico: timing and composition of the southernmost edge of the
1590 Jurassic continental arc. *Canadian Journal of Earth Sciences*, 61(1), 117-133.
1591 <https://doi.org/10.1139/cjes-2023-0059>
- 1592
- 1593 Valentine, W. G. (1936). Geology of the Cananea Mountains, Sonora, Mexico. *Bulletin of*
1594 *the Geological Society of America*, 47(1), 53-86. <https://doi.org/10.1130/GSAB-47-53>
- 1595
- 1596 Varela, F. E. (1972). *Tourmaline in the Cananea mining district, Sonora, Mexico: Unpub.*
1597 M.S. Thesis, University of California, Berkeley, 79 p.
- 1598
- 1599 Vega-Granillo, R., and Calmus, T. (2003). Mazatan metamorphic core complex (Sonora,
1600 Mexico): structures along the detachment fault and its exhumation evolution. *Journal of*
1601 *South American Earth Sciences*, 16(4), 193-204. [https://doi.org/10.1016/S0895-](https://doi.org/10.1016/S0895-9811(03)00066-X)
1602 [9811\(03\)00066-X](https://doi.org/10.1016/S0895-9811(03)00066-X)
- 1603
- 1604 Vermeesch, P. (2018). IsoplotR: A free and open toolbox for geochronology. *Geoscience*
1605 *Frontiers*, 9(5), 1479-1493. <https://doi.org/10.1016/j.gsf.2018.04.001>
- 1606

- 1607 Virtue, T. L. (1996). *Geology, mineralogy, and genesis of supergene enrichment at the*
1608 *Cananea porphyry copper deposit, Sonora, Mexico*. Unpublished M.Sc. Thesis, The
1609 University of Texas at El Paso, 284 p.
- 1610
- 1611 Wernicke, B. (1992). Cenozoic extensional tectonics of the US Cordillera. *The Geology of*
1612 *North America*, 3, 553-582. <https://doi.org/10.1130/DNAG-GNA-G3.553>
- 1613 Whitmeyer, S.J., and Karlstrom, K. (2007). Tectonic model for the Proterozoic growth of
1614 North America. *Geosphere*, 3(4), 220–259. <https://doi.org/10.1130/GES00055.1>
- 1615
- 1616 Williams, T. J., Candela, P. A., and Piccoli, P. M. (1995). The partitioning of copper between
1617 silicate melts and two-phase aqueous fluids: an experimental investigation at 1 kbar, 800 C
1618 and 0.5 kbar, 850 C. *Contributions to Mineralogy and Petrology*, 121, 388-399.
1619 <https://doi.org/10.1007/s004100050104>
- 1620
- 1621 Wodzicki, W. A. (2001). The evolution of magmatism and mineralization in the Cananea
1622 district, Sonora, Mexico. *Special Publication-Society of Economic Geologists*, 8, 243-264.
1623 <https://doi.org/10.5382/SP.08.15>
- 1624
- 1625 Wodzicki, W. A. (1995). *The evolution of Laramide igneous rocks and porphyry copper*
1626 *mineralization in the Cananea district, Sonora, Mexico*. Unpublished PhD dissertation,
1627 University of Arizona, Tucson, pp. 181.
- 1628
- 1629 Wones, D. R. (1989). Significance of the assemblage titanite+ magnetite+ quartz in granitic
1630 rocks. *American Mineralogist*, 74(7-8), 744-749.
- 1631
- 1632 Wong, M. S., and Gans, P. B. (2003). Tectonic implications of early Miocene extensional
1633 unroofing of the Sierra Mazatán metamorphic core complex, Sonora,
1634 Mexico. *Geology*, 31(11), 953-956. <https://doi.org/10.1130/G19843.1>
- 1635
- 1636 Wong, M. S., Gans, P. B., and Scheier, J. (2010). The $^{40}\text{Ar}/^{39}\text{Ar}$ thermochronology of core
1637 complexes and other basement rocks in Sonora, Mexico: Implications for Cenozoic tectonic
1638 evolution of northwestern Mexico. *Journal of Geophysical Research: Solid Earth*, 115(B7).
1639 <https://doi.org/10.1029/2009JB007032>

1640

1641 Zhang, X., Guo, F., Zhang, B., Zhao, L., Wu, Y., Wang, G., and Alemayehu, M. (2020).
1642 Magmatic evolution and post-crystallization hydrothermal activity in the early Cretaceous
1643 Pingtan intrusive complex, SE China: Records from apatite geochemistry. *Contributions to*
1644 *Mineralogy and Petrology*, 175, 1-18. <https://doi.org/10.1007/s00410-020-1675-2>

1645

1646 Zhao, H., Wang, Q., Li, W., Shu, Q., Sun, X., and Deng, J. (2022). The roles of emplacement
1647 depth, magma volume and local geologic conditions in the formation of the giant Yulong
1648 copper deposit, Eastern Tibet. *Ore Geology Reviews*, 145, 104877.
1649 <https://doi.org/10.1016/j.oregeorev.2022.104877>

1650 HIGHLIGHTS

- 1651 - Zircon U-Pb dating of the ore-related porphyries indicates a life span of at least ~4 Myr
1652 for the magmatic activity related to the mineralization processes at the Buenavista del
1653 Cobre deposit
- 1654 - At least two magmatic cycles involving fractional crystallization of plagioclase at depth
1655 are associated with the formation of the giant Buenavista del Cobre deposit
1656 mineralization.
- 1657 - Apatite geochemistry can be used as an exploration tool to differentiate ore-rich from
1658 ore-poor porphyry intrusions analyzing apatite REE signatures.

1659